

Persistent, “Mysterious” Seismoacoustic Signals Reported in Oklahoma State during 2019

Joshua D. Carmichael¹, Andrew D. Thiel², Phillip S. Blom¹, Jacob I. Walter², Fransiska K. Dannemann Dugick³, Stephen J. Arrowsmith⁴, and Chris G. Carr¹

ABSTRACT

We report on the source of seismoacoustic pulses that were observed across the state of Oklahoma (OK) during summer of 2019, and the subject of national media coverage and speculation. Seismic network data collected across four U.S. states and interviews with witnesses to the pulse’s effect on residential structures demonstrate that they were triggered by routine ammunition disposal operations conducted by McAlester Army Ammunition Plant (McAAP). During these operations, conventional explosives destroy obsolete munitions stored in pits through a controlled sequence of electronically timed shots that occur over tens of minutes. Despite noise-abatement efforts that reduce coupling of acoustic energy with air, some lower frequency, subaudible (infrasonic) sound radiates from these shots as discrete pulses. We use nine months of blast log documents, seismic network records, analyst picks, and physical modeling to demonstrate that seismic stations as far as 640 km from McAAP sample these pulses, which record seasonal patterns in stratospheric and tropospheric winds, as well as the dynamic formation of waveguides and shadow zones. Digital short-term average to long-term average detectors that we augment with dynamic thresholds and time-binning operations identify these pulses with a fair probability, when compared with visual observations. Our analyses thereby provide estimates of observation rates for both partial and full sequences of these pulses, as well as single shots. We suggest that disposal operations can exploit existing, composite seismic networks to predict where residents are likely to witness blasting. Crucially, our data also show that dense seismic networks can record multiscale atmospheric processes in the absence of infrasound arrays.

KEY POINTS

- “Mysterious” seismoacoustic pulses reported by media are sourced by munition explosions in Oklahoma.
- Dense seismic networks record these pulses to reveal multiscale and seasonal atmospheric wind patterns.
- Seismic energy detectors process this network data to quantify and bound residential observation probabilities.

[Supplemental Material](#)

INTRODUCTION

In July 2019, researchers at the Oklahoma Geological Survey (OGS) documented an unusual observation in their field blog: seismic stations distributed over Oklahoma (OK) and neighboring U.S. states had recorded sequences of repetitive, quasi-similar signals almost daily over the previous spring and summer months (Thiel, 2019). These signals appeared after 16:00 UTC (11:00 local time) in the 0.3–20 Hz frequency band as wavetrains of short duration pulses (~1–3 s pulse widths) that were separated by 20 s intervals, and moved near

acoustic propagation speeds over widespread regions of OK and Texas (TX). The onset of a wavetrain at a particular station was generally marked by two pulses that were separated by 20 s, followed by a delay of ≤ 80 s, and proceeded 24 subsequent pulses, each separated in time again by integer multiples of 20 s. This full pattern often repeated after 120 s, so that seismic data recorded by a given station could show 52 pulses over a total duration that met or exceeded 1200 s (20 min; Fig. 1). Conventional location algorithms that consumed analyst phase picks and employed seismic-velocity models generally

1. Los Alamos National Laboratory, Geophysics Group, Los Alamos, New Mexico, U.S.A.,  <https://orcid.org/0000-0001-5752-5738> (JDC);  <https://orcid.org/0000-0002-9273-8584> (CGC); 2. Oklahoma Geological Survey, University of Oklahoma, Norman, Oklahoma, U.S.A.,  <https://orcid.org/0000-0001-7127-9422> (JIW); 3. Sandia National Laboratories, Geophysical Detection Programs, Albuquerque, New Mexico, U.S.A.,  <https://orcid.org/0000-0001-8328-4835> (FKDD); 4. Roy M. Huffington Department of Earth Sciences, Southern Methodist University, Dallas, Texas, U.S.A.,  <https://orcid.org/0000-0002-9150-0363> (SJA)

*Corresponding author: joshuac@lanl.gov

Cite this article as Carmichael, J. D., A. D. Thiel, P. S. Blom, J. I. Walter, F. K. D. Dugick, S. J. Arrowsmith, and C. G. Carr (2021). Persistent, “Mysterious” Seismoacoustic Signals Reported in Oklahoma State during 2019, *Bull. Seismol. Soc. Am.* **XX**, 1–22, doi: [10.1785/0120210145](https://doi.org/10.1785/0120210145)

© Seismological Society of America

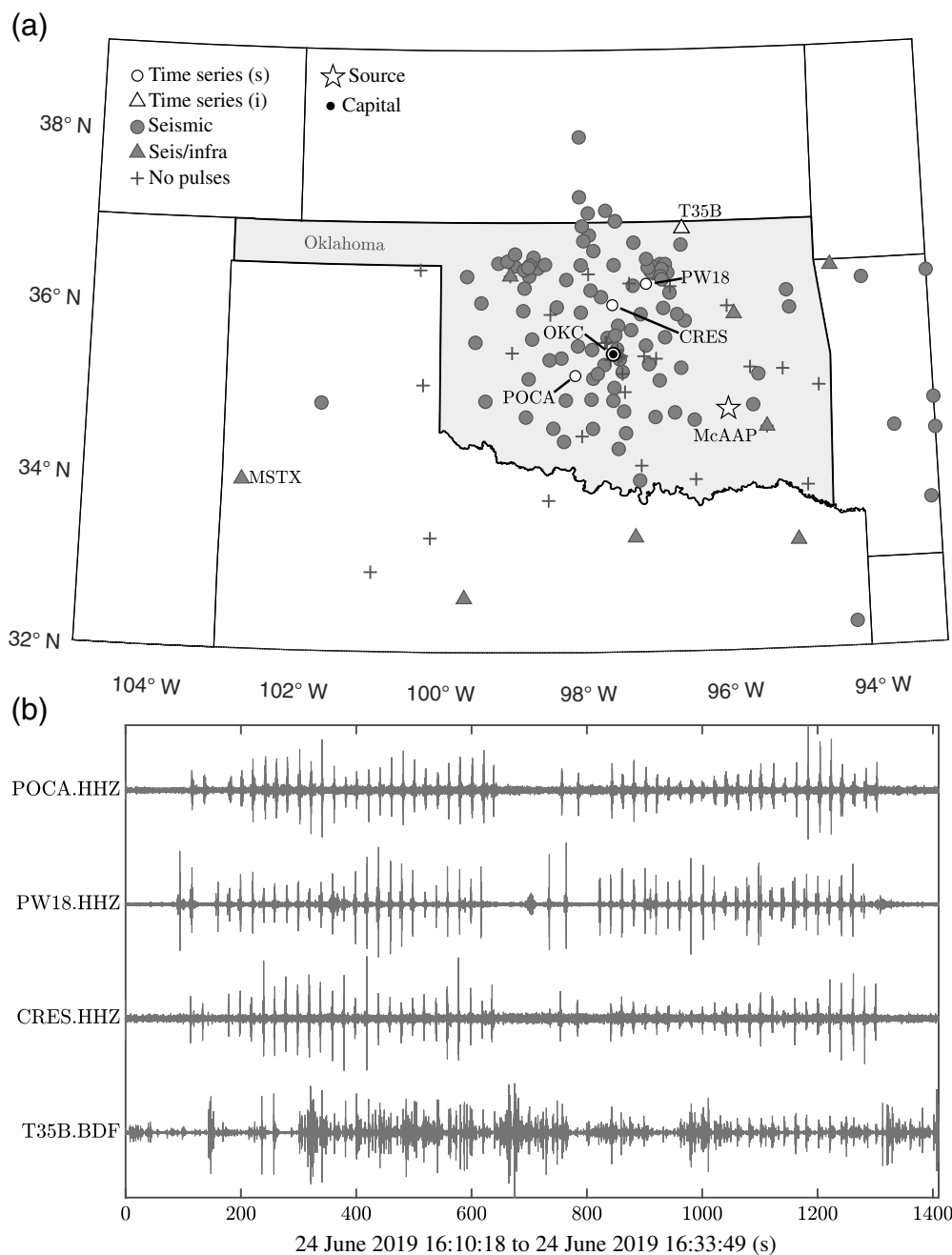


Figure 1. Seismoacoustic sensors and records of demolition explosions sourced at McAlester Ammunition Plant (McAAP) from 18 February to 20 November 2019, near the state of Oklahoma. (a) Seismic stations (circles) and codeployed seismic (s) and infrasound (i) sensors (triangles) that record pulse sequences, with the three seismograms in (b) highlighted (white circles or triangles). Crosses mark stations with no pulse sequence observations. Additional labels show the most remote station MSTX (~640 km away), McAAP (star), and Oklahoma City (OKC) (coincident circles). Supplement S1 documents network, sensor, digitizer, sampling interval, and modem type for each station, where available (Sheet C). (b) A subset of band-pass filtered (5–15 Hz) wavetrains recorded after 24 June 2019 16:10:19 (UTC) on three seismic stations (channel HHZ shown) and a single infrasound sensor (T35B.BDF). The seismograms clearly show pulse sequence patterns that repeat once. Each wavetrain begins with a pair of two pulses, separated by 20 s, followed after ~80 s by an additional 24 pulses each separated by 20 s (roughly between 0 and 600 s). The second wavetrain appears about 120 s after the first (roughly between 700 and 1220 s). The infrasound record of the pulse sequence (the most obvious between 1000 and 1200 s) is more muted by background noise and interference than the seismic records. We intranormalized each seismic waveform so that peak amplitude of PW18 is 7 × that of POCA, and CRES is 1.5 × that of POCA. The infrasound peak amplitude is also about 7 × that of POCA.

produced divergent or nonsensical epicentral solutions. A more manual moveout analysis by OGS researchers subsequently showed that pulses propagated across the network at expected infrasound celerities (epicentral distance divided by total travel time) of 240–345 m/s, rather than at seismic wavespeeds. This analysis also revealed that pulse presence was spatially inconsistent; the number and distribution of seismic stations that recorded these pulses above background noise varied daily but could not be explained by changes in this background noise. Further, although these wavetrains were not observed above noise by all stations daily, they were never recorded on a Sunday.

These cumulative observations constrained both source identity and emplacement. Specifically, the regularity in wavetrains' onset, their temporal duration, and the absence of such signals on Sundays suggested that the pulses timed with a work schedule. The phase speed and inconsistency in pulse amplitude further suggested that the OGS seismometers had recorded infrasonic waveforms (seismoacoustic signals) that had propagated from near-surface, anthropogenic sources that were not seismically coupled to the ground. If these sources were on the ground, then the broad spatial distribution of sensor observations implied that energy had instead propagated long distances through atmospheric waveguides created by wind and temperature gradients in the troposphere (near ground) and stratosphere (above the troposphere) (Garcés *et al.*,

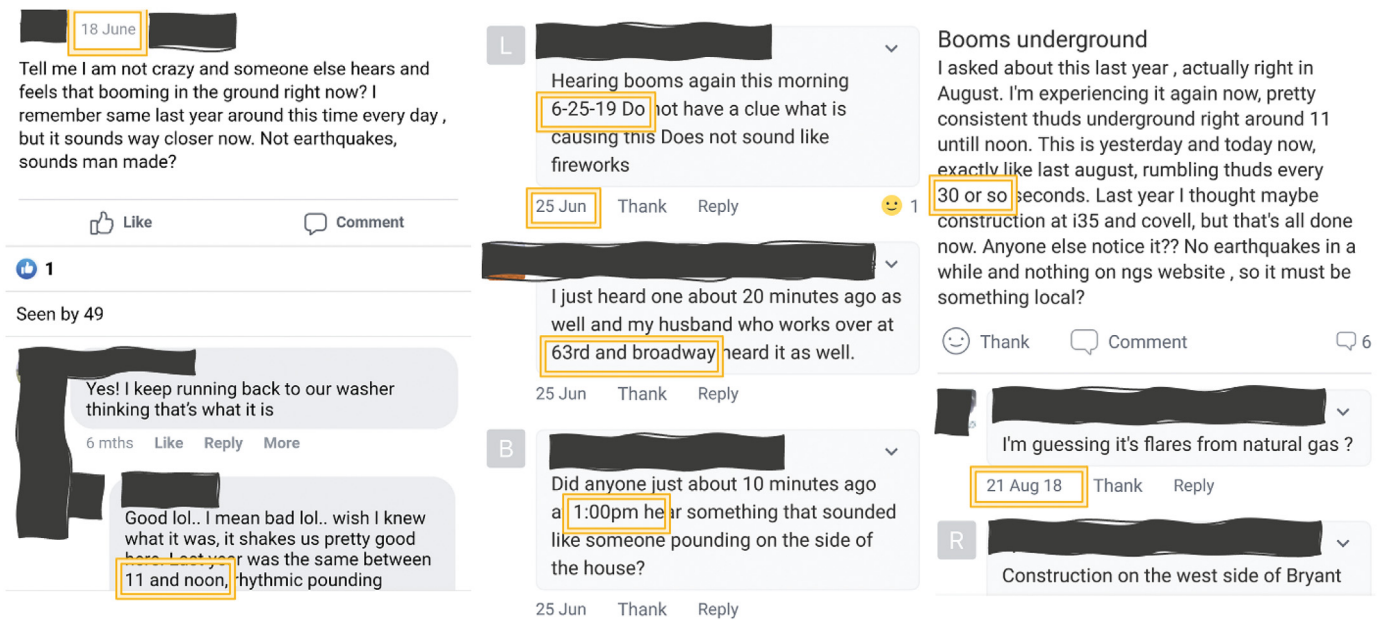


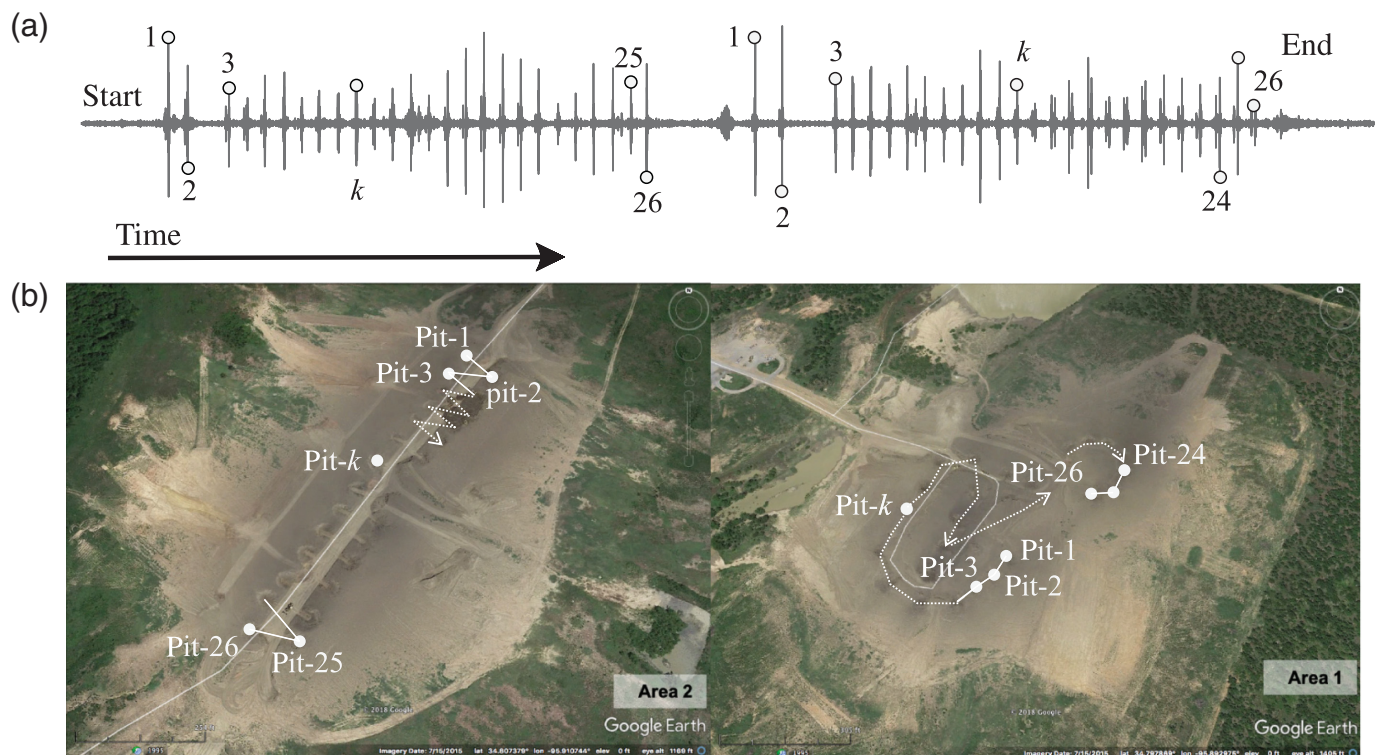
Figure 2. Samples of social media posts authored by residents of Edmond, OK, dated 18 June 2019, 25 June 2019, and 21 August 2019. The posts document auditory and physical reports of explosions that are almost certainly sourced at McAAP. Black ribbons obscure identity of users, and yellow rectangular frames highlight metadata.

1998). Tropospheric temperature gradients would then refract energy upward into these atmosphere layers, whereas wind structures in the tropospheric jet stream and stratospheric, circumpolar vortex would refract this energy downward to the ground again. Direct loading of the ground by the incident pressure front at these ground intercepts that collocate with seismometers then provide a physical mechanism to couple infrasound energy into seismic ground motion, as documented in the explosion- and bolide-monitoring literature (e.g., Nickel and Whitaker, 1971; Kitov *et al.* 1997; Edwards *et al.*, 2008; Aleqabi *et al.*, 2016). A search for acoustic array deployments that could provide data to better detect and localize such sources revealed that only 10 spatially separated infrasound stations in OK, west Arkansas (AR), or north TX were online between winter and summer of 2019. Of these stations, only T35B that was codeployed with a high-frequency seismic station routinely recorded the pulses (Fig. 1). Absent of infrasound array data and guided by reports of similar signals (Negru *et al.*, 2010), OGS researchers then initiated contact with energy pipeline operators, community leaders, and local military bases. This outreach revealed that residents near Oklahoma City (OKC) had coincidentally observed “banging” sounds after 16:00 UTC throughout the summer that they reported to police and over neighborhood social media platforms (Fig. 2). Other residents and business owners had submitted inquiries to the Oklahoma Corporation Commission, who then shared their data. This information eventually led researchers to determine that the waveforms recorded by the OGS and other networks had captured explosions sourced by routine munition disposal operations located at the McAlester Army Ammunition Plant (McAAP), located ~180 km east of OKC. Publicly accessible imagery (Fig. 3) further showed that the McAAP disposal complex (34.804, -95.904) includes two sites (area 1 and area 2) separated by ~2 km that each hosts 26 individual shot pits,

and that can accommodate a total of 52 disposal articles (Supplement S1; Sheet A and Sheet D, available in the supplemental material to this article). The number and spatial distribution of these shot pits generally explained the pulse patterns recorded on the OGS stations (two, time-separated patterns of 26 pulses; Fig. 3) and confirmed the source identity of the wavetrains. Moveout estimates that included McAAP as the source origin additionally confirmed that the OGS network had recorded seismoacoustic waveforms with expected tropospheric and stratospheric propagation speeds, rather than seismic waveforms (Fig. 4).

Although the OGS researchers established that McAAP was the source of these wavetrains, their conclusions were not widely known. Rather, reports of mysterious booms in popular science media (Wei-Haas, 2019), documentation of pulse observations by OK residents (Fig. 2), and ground-based measurements collected as far as ~640 km from McAAP (station code MSTX, Fig. 1) were still covered media and popular science literature (Carmichael, 2019b). These data also raise geophysical questions: namely, how multiscale atmospheric variability controls the observability of quasi-repeatable sources of infrasound energy.

This article combines a ground-truth dataset that logs nine months of operations at McAAP, manual seismometer observations, predicted ground arrivals from an infrasound propagation model, and digital detection statistics of pulse sequences to make three significant contributions to seismoacoustic



research. First, we provide a dense, manually digitized, and visually reviewed dataset that documents more than 7.2×10^3 explosions and 2.4×10^4 seismogram reviews to serve as ground truth for future geophysical studies of seismoacoustic propagation. This first contribution will enable researchers to easily access our data and study variability within the atmosphere, which we do not do. Second, we show that dense seismometer networks can capture multiscale variability of infrasound arrivals that we assert shows seasonal patterns in stratospheric and tropospheric winds. This second contribution means that seismic sensors are sufficient to make binary detections (arrival versus no arrival) of seasonal changes in wind direction, absent of infrasound arrays, at least in some scenarios. Third, we show that augmented baseline short-term average to long-term average (STA/LTA) detectors that process seismometer data can identify the majority of visibly confirmed pulse sequences sourced at McAAP, even after accounting for false alarms sourced by background seismicity or noise. This third contribution means that automated processing of seismic network data provides a fair-to-moderate (defined later) detection capability of McAAP blasting operations, up to 640 km from the source. Our subsequent analyses of these data provide additional summary statistics of pulse sequence detections and show that a majority of regions within the 640 km distance that include seismometer deployments will witness a full sequence of pulses sourced at McAAP at least once over the course of a year like 2019, and that most regions will witness at least one pulse per blasting sequence.

The volume of waveforms recorded during this nine-month study period that required manual review to document ground

Figure 3. (a) A notional record of a pulse sequence from Figure 1, with enumerated pulse counts from “start” to “end” to indicate 52 distinct explosion sources that locate between area 2 (left) and area 1 (right). (b) Images gathered from the Google Earth show area 1 and area 2 within the McAAP complex that are in various stages of maintenance. Select pits are marked to associate with the pulse sequence record in (a). Each area includes 26 shot pits that disposal teams can access from either a linear road (area 2) or a circular road (area 1). Disposal pits include three-sided berms and are separated from neighboring pits by roughly 30 m. Each pit accommodates the disposal of a soil-covered article that is destroyed with electronically timed, conventional explosives. The maximum distance between any two pits within area 1 is 240 m, with the long pit-axis oriented at an $\sim 30^\circ$ azimuth. The maximum distance between any two pits within area 2 is also 285 m, with the long pit-axis, again oriented at $\sim 30^\circ$ azimuth. Area 2 is ~ 2 km northwest of area 1. Dashed arrows indicate the consistent, sequential order of blasting. The marker labeled pit-26 on the far right marks the last shot location in Area 1. Supplement S1 (Sheet D) documents precise geographical locations for each area and certain shot pits.

truth also limited the scope of our analyses. We do not invert for infrasound source locations, perform a long-term noise study at each sensor, or present daily comparisons between propagation model output and pulse observations as done in other studies that exploit fewer sources (Dannemann-Dugick *et al.*, 2020). We also do not combine seismic and infrasound data (where available), although several studies demonstrate that such data stream and catalog fusion efforts increase signal detection rates (Albert and Arrowsmith, 2017; Carmichael *et al.*, 2020) and reduce source parameter estimation variability (McKee *et al.*, 2018; Koch and Arrowsmith, 2019; Williams *et al.*, 2021). Nonetheless, our visual observations and digital detection probabilities that

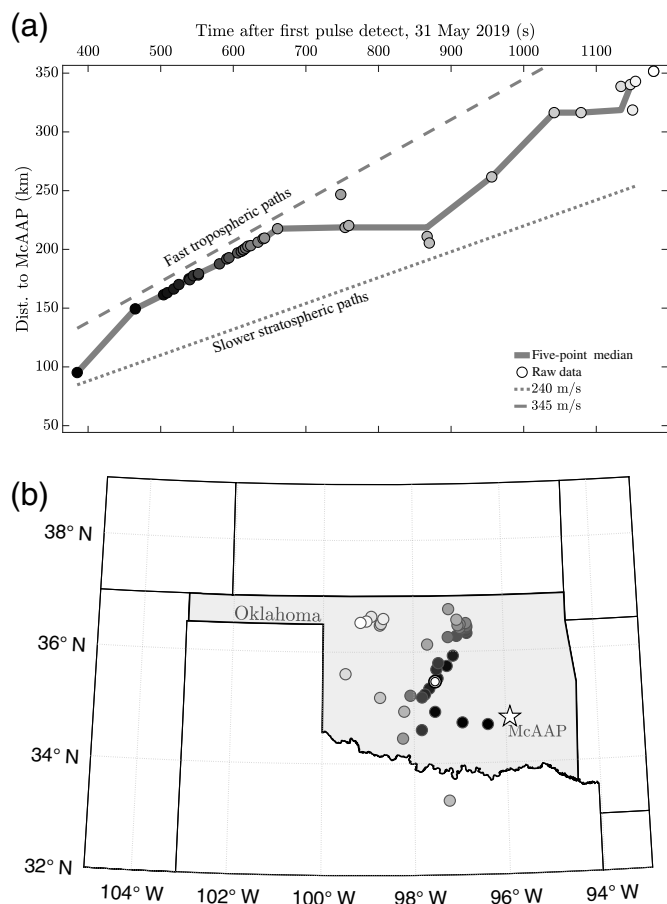


Figure 4. (a) A moveout plot that shows time delays between the earliest first-pulse observed in a wavetrain at a given station and the first pulse observed in a wavetrain at subsequent stations. The vertical axis shows the distance between each station and McAAP (marked with a star). The solid curve shows moving, five-point median time delays versus moving, five-point median distance measurements. Dashed curves show fast, tropospheric moveout speeds (345 m/s) and slower stratospheric moveout speeds (240 m/s). (b) Filled circles mark stations corresponding to the moveout in (a), so that earliest pulse arrivals are dark and indicate a source to the southeast. A capital city symbol (a white circle superimposed on a dark circle) marks OKC.

account for false alarms are quantitatively defensible, and can thereby inform blasting operations on where and when observers will most likely report activity at McAAP. Further, the comprehensive and accessible format of our novel dataset will enable research on multiscale atmospheric variability that may otherwise be difficult to conduct without these resources.

DATA AND STUDY REGION

Source data (ground-truth blast logs)

We obtained blast logs for articles that were destroyed at the McAAP disposal complex between 19 February and 20 November 2019 through a Freedom of Information Act request. These logs document metadata that include time stamps that various articles of a given cumulative mass were destroyed within shot pits at a given area (in lbs), Federal

Aviation Administration (FAA) weather conditions at the time of disposal, and the total number of shots. Disposal procedures require that demolition experts destroy articles in shot pits that are each buttressed by three berms and then buried under a soil load that (partially) decouples the explosion from the air (Calderone and Garbin, 2001). Operators then electronically fire two shots to determine if peak overpressure exceeds prescribed thresholds, prior to proceeding with subsequent shots ~ 80 s later. These subsequent shots spatially order from a consistent start point to an end point in either a zig-zagged, clockwise pattern (area 1), or a sequential, north-south zig-zag pattern (area 2; Fig. 3b). The blast logs show that McAAP conducted a minimum of two shots (once; 9 May 2019) and maximum of 52 shots per day, and therefore exceeded threshold overpressures at the most once. The cumulative mass destroyed by these shots on any blasting day ranged from 224 lbs ($\sim 10^2$ kg) to 117,210 lbs ($\sim 5.3 \times 10^4$ kg). The larger of these operations (more mAU: Can it bbe ass destroyed) often split disposal between area 1 (34.79785, -95.89371) and area 2 (34.80882, -95.90994). The smaller of these operations (less mass destroyed) generally located at one area, with a slight majority (12%) of such single-area shots conducted at area 2; these smaller operations also often required less than 26 shots. Logged disposal operations at one area initiated between 300 and 1140 s after operations started at another area, with a median separation of time of 660 s; we note that a full 26 shot sequence lasted ≤ 600 s at each 26 shot-pit area. To better review and access these data, we digitized these blast logs into spreadsheets and indexed disposal and weather information by both time and area (Supplement S1). We further summed disposal mass and the associated number of shots over monthly time bins (Fig. 5a). Area 2 logs from one day (12 April 2019) documented shots but excluded a time stamp. Logs from another day with ostensibly scheduled blasting (17 September 2019) appear blank. In these cases, we imputed the logged area 1 shot time into the area 2 shot log (12 April) or assumed a start time of 16:00 UTC (17 September). Overall, the remaining data revealed that McAAP destroyed between ~ 128 and 581 t (metric tons) of munitions using 254–988 individual shots per month, depending on the month (Fig. 5b).

Instrument deployments

The 145 seismic stations (including 30 Raspberry Shakes) deployed across four U.S. states (AR, Kansas or KS, OK, and TX; Fig. 1) between 19 February and 20 November 2019 comprised 11 different seismic networks that operated ≥ 11 distinct sensor types, digitizing data at ≥ 3 sampling intervals with at least five distinct data loggers. Three or more distinct modems facilitated data telemetry. Deployment distances from McAAP ranged from 32.5 km (station code R4495) to nearly 640 km (station code MSTX), with stations as far north as 38.00° latitude, as far south as 32.29° , as far east as -92.80° , and as far west as -102.77° . Station elevations ranged from 62 to 1169 m above sea

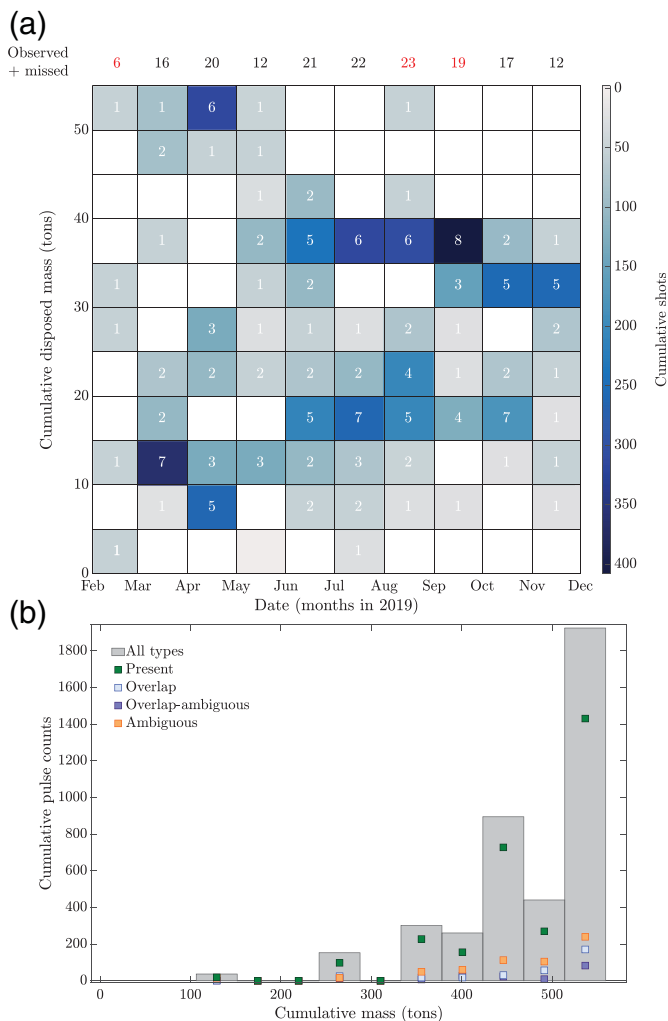


Figure 5. (a) A summary of blast log data shown as a 2D histogram, superimposed on visual pulse sequence observations (numbered bins). The vertical axis discretizes mass destroyed into 11 bins, and the horizontal axis discretizes time into monthly bins; vertical lines mark the start of each month. Bin color indicates the total number of shots conducted in a given month, within a given mass bin. Integers marking colored bins count the total number of days with records of a pulse sequence observation within that month and within a given mass interval. The row of integers above the largest mass bin counts the total number of days with any visible pulse sequence observation within that month bin. Red counts indicate that a month included a missed visual detection, which never exceeded one. For example, the unique bin marked with 8 indicates that we observed pulse sequences (with any typology) during eight days of September, in which about 400 shots destroyed between 35 and 40 t of mass. The sum of counts along this column is 18; the red 19 above the September-to-October column, therefore, indicates an absence of pulse sequence observations at any station, during one day of blasting. (b) Cumulative, binary pulse sequence observations (counts) summed over stations with visual observations (vertical axis) versus cumulative mass destroyed (horizontal axis) at both areas, each summed over monthly time bins and displayed with pulse sequence typology (square markers). The number of pulse sequence observations increases with disposal mass, but shows variability. Plots that use cube-root scaling of charge mass reveal similar relationships (not shown).

level. The mean azimuthal gap was 2.12° and peaked at 27.45° , with a large density of stations deployed northwest of McAAP relative to the total. Radial density of stations peaked at roughly 160 km from McAAP, with over 50% of all stations in our composite network deployed within the annulus spanning 120–230 km from the explosive disposal complex. Other networks operated stations within our geographical bounding box that remained embargoed through 2019 and into 2020 when we collected our metadata from the Incorporated Research Institutions for Seismology (IRIS) website (see [Data and Resources](#)). We were, therefore, unavailable to access these records and restricted processing to stations in the IRIS “_REALTIME” network; we note that stations often belong to multiple networks.

This bounding box for the seismic deployment also included 10 stand-alone infrasound stations or Raspberry Booms (no arrays), which we occasionally reviewed, but did not routinely process (Fig. 1, triangular markers). Our Supplement S1 documents the individual station instrumentation details in a comprehensive table (Sheet C).

METHODS AND RESULTS

Manual waveform observations

Our digitized blast log data showed that McAAP blasted on 169 of the total 276 days elapsed between 18 February and 20 November 2019 (~75% of days). To identify any associated blasting signatures on seismic receivers, we visually reviewed all vertical channel seismograms recorded over this date range. This review included a 2.5 hr duration period time window that followed the first documented blast, after correcting from the local time zone (which observes daylight savings time). We further split our review tasks into two compartmentalized teams (team 1 and team 2) that independently reviewed all available seismic and (some) infrasound receivers for consecutive, seismoacoustic pulses separated by integer multiples of ~ 20 s; this split was intended to reduce effects of analyst bias on visual detection rates. Both teams thereby accessed vertical channel seismic-waveform data recorded on ≤ 145 seismic stations distributed across four U.S. states (AR, KS, OK, and TX), over time windows that began ~ 60 s before the first logged blast time, and that extended 4140 s or more after this start time. Team 1 examined every available Raspberry Shake station on every day and most stations on all the other days. Team 1 also made occasional phase arrival moveout measurements (Supplement S1, Sheet D). Team 2 examined every available non-Raspberry Shake station on every day, occasionally reviewed infrasound station data (additional to seismometer records), but made no manual moveout measurements. Both teams examined some data during days with no logged blasting to quantify any false visual detections (Supplement S1, Sheet A).

Each team independently selected filter bands to preprocess data prior to visual review. Team 1 researchers filtered seismograms between 0.7 and 20 Hz, and visually graded any

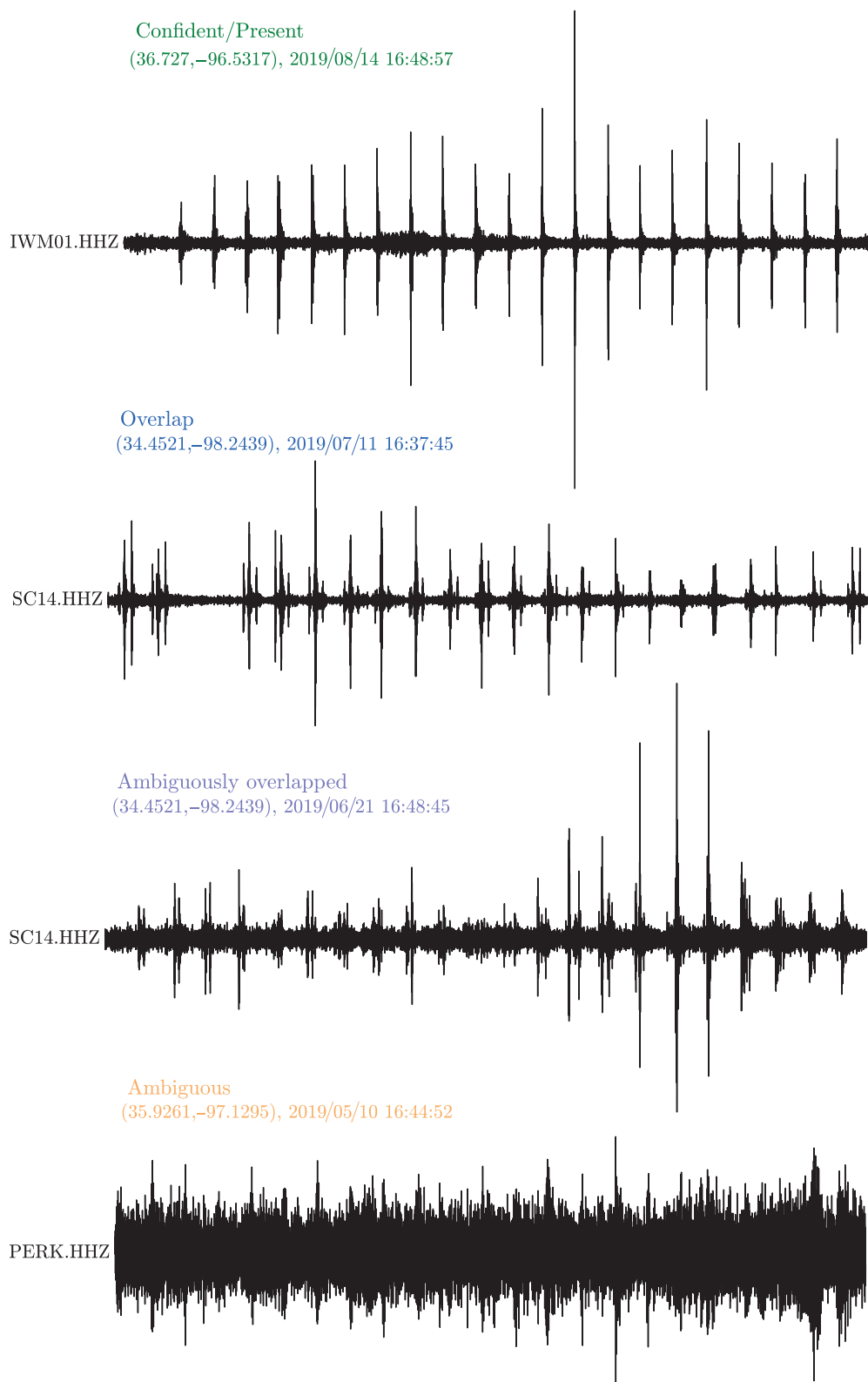


Figure 6. Pulse sequence examples for 450 s of data, labeled with the station code and typologies (present, overlapped, ambiguously overlapped, and ambiguous). The color of the typology, geographic location, and dates match the coding of our spreadsheet resource (Supplement S1, Sheet B). The record time labels do not show the start time of the time series but the beginning of each 4120 s length data record that includes these data, as described in the [Manual Waveform Observations](#) section.

wavetrain observations on each station with four possible indicators: (1) present (or confident), (2) overlap, (3) ambiguous, and (4) ambiguously overlapped. Team 1 further marked the absolute arrival time of pulses within a wavetrain to measure moveout when the first pulse in a given sequence was unambiguously observable, on certain days. Each of these four pulse sequence typologies, although unavoidably subjective, followed certain criteria (Fig. 6):

1. “Present” or “confident” indicates at least four, high signal-to-noise ratio (SNR) waveforms separated by consecutive integer multiples of approximately 20 s.
2. “Overlap” indicates at least four, high SNR waveforms separated by consecutive integer multiples of approximately 20 s that interleave with similarly spaced signals.
3. “Ambiguous” indicates either (1) an unclear first pulse within a sequence of four or more waveforms that separate by integer multiples of approximately 20 s or (2) four pulses that separate by integer multiples of 20 s, which could skip multiples (e.g., two consecutive pulses separate by 60 s rather than 20 s).
4. “Ambiguous overlap” indicates either: (1) data visibly include two interleaved wavetrain sequences, in which the primary and secondary pulse sequences are not clearly separated in time, or (2) interleaved wavetrains in which the primary or secondary pulse sequences exhibit low SNR.

Team 2 filtered data between 5 and 15 Hz prior to visual review, and graded pulse sequences using the same scheme as team 1. Waveforms often visually showed greater SNR in this band at most stations, and one team's grade occasionally contradicted that of the other. In these cases, we labeled each station with a final grade associated with the highest SNR observations and at least one team reviewed every available seismic station, at least once. Each team only occasionally observed overlapped or ambiguously overlapped pulse sequences that included signals from more than two interleaved wave-trains (e.g., three or more pulses per shot; SC14, Fig. 6). Of the 145 available seismic stations, 25 stations recorded no pulse sequences of any typology during review (cross marks, Fig. 1), so that 120 seismic stations total observed at least one pulse sequence during the approximately nine-month collection period. Supplement S1 (Sheet B) documents the complete date- and station-resolved grading of each pulse sequence with color coding.

We note that some disposal operations involved fewer than four shots (9 May, 2019). Because our scheme required four or more consecutive pulses to grade an observation of any kind, we did not visually detect true pulse sequences sourced by such operations.

Observation typology statistics

Our manual grading identified pulse sequences on at least some stations for all but three days that our blast logs recorded munition disposal (three red counts in Fig. 5a). Collectively, this process counted $\sim 5 \times 10^4$ time-separated pulses that were sourced by 7222 shots located at McAAP. To determine the relative frequency that sensors recorded seismoacoustic blasting signatures, we discretized network-station codes into 12 bins that measure the fraction of days that at least one of the two teams recorded a pulse sequence of any typology (Fig. 7a), excluding two days with possible false alarms (Supplement S1, Sheet A). The most populous of our 12 bins included 24 stations that produced pulse sequence observations during a total of one-to-eight days. On average, bins included 10 stations, and a minimum of three sensors provided observations among all bins. Three such stations (two Streckeisen STS-2 and one Güralp CMG-3T with codes MRSH, POCA, and SC14) that were deployed between 202 and 220 km west of McAAP, and with interstation separation distance ≥ 100 km, recorded pulse sequences during 53%–59% of all days with logged blasting activity. These are, therefore, the most reliable sensors (two Streckeisen STS-2 and one Güralp CMG-3T) for visually observing seismoacoustic signals sourced at McAAP.

Confident observations of pulse sequences accounted for more than 73% of all identified blasting signatures in the record (Fig. 7b). This was followed by ambiguous ($\sim 15\%$), overlapping ($\sim 8\%$), and ambiguously overlapping ($\sim 4\%$) typologies. Sensors at POCA and SC14 recorded a particularly large fraction of interleaved (overlapping) pulse sequences that

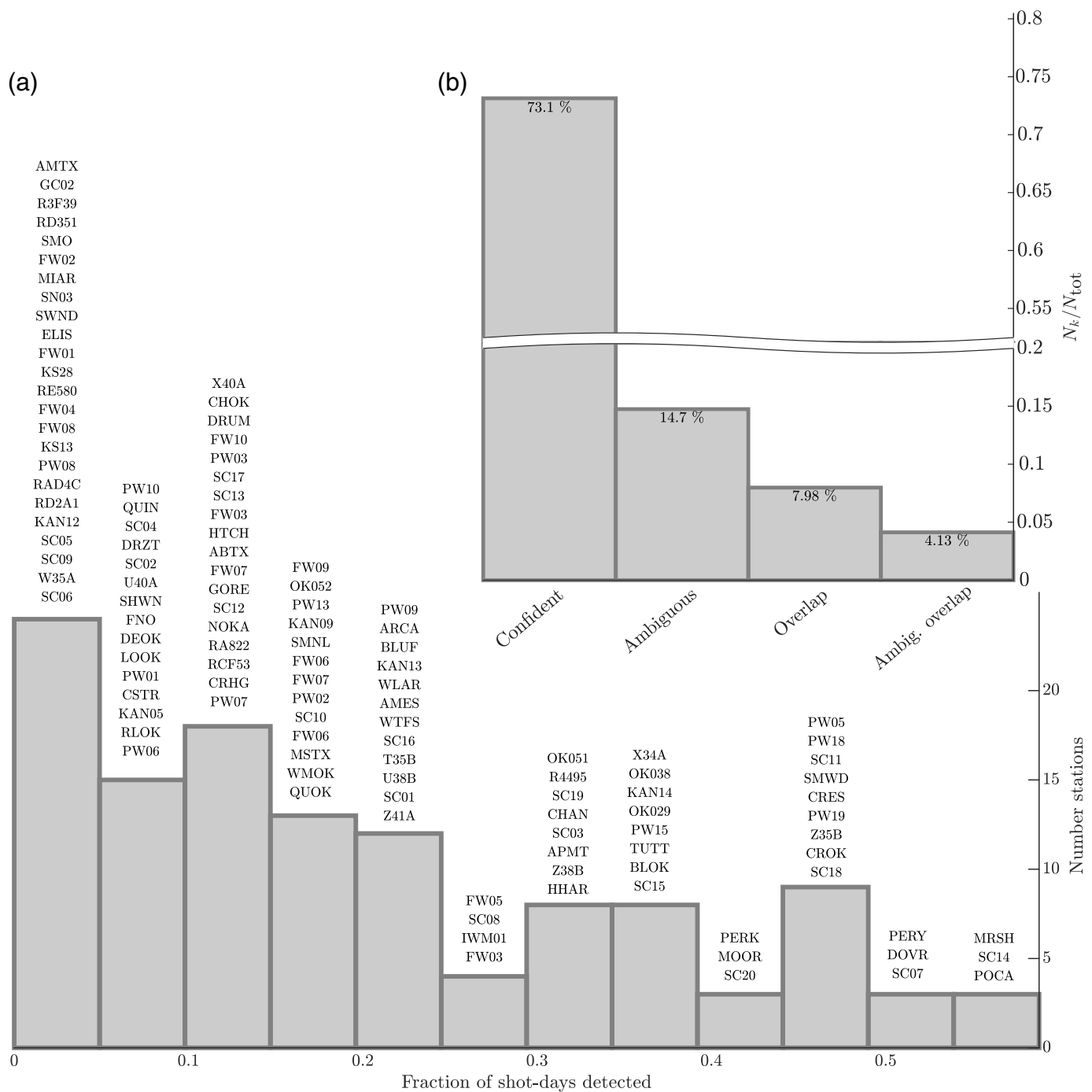
almost certainly indicate infrasonic multipathing in the atmosphere, and likely increased the probability that seismograms contained visible signatures of blasting at McAAP. Our Supplement S1 includes a higher resolution time series of observations, indexed by typology (Sheet B, Fig. S1-1). Although number of sensors with pulse sequence observations often increased with disposed mass (Fig. 5a), spatial patterns of pulse observations of any typology on particular days also appeared farther westward, more spatially extensive, and more numerous during summer than in winter or fall (Fig. 8; Supplement S2).

Comparison with Oklahoma resident observations

Our time history of visual pulse observations fortuitously coincided with physical observations by certain OK residents. One such observer (observer A) in Edmond, OK, that resided 170 km from McAAP in 2019 (zip code 73034) made informal auditory reports of explosions (sometimes documented as "booms") over social media platforms between 18 June and 22 August 2019 (Fig. 2). Observer A shared screenshots of these posts with us, which are time-tagged as 18 June 2019, 25 June 2019, 21 August 2019, and 22 August 2019, and delivered written documentation of the posts' details on 9 December 2019 with authorization to share their content. In detail, at least 11 of observer A's neighbors within hundreds of meters to several kilometers of their home responded that they had also heard, or felt, repetitive signals that are qualitatively consistent with the timing and duration of pulse sequences sourced at McAAP. One neighbor also contacted their spouse at their place of employment 26 km away in OKC, who additionally reported hearing signals from that location. Observer A and their neighbors consistently described the sounds as a "pounding" or "thuds" on the exterior of their houses with these social media posts. One neighbor counted 30 of the pulses, and assumed that their washing machine was off balance and was the source of the signals. Another neighbor estimated the interevent time of "booms" to be 30 s; we note that McAAP demolition shots occur with electronically defined separation times of 20 s.

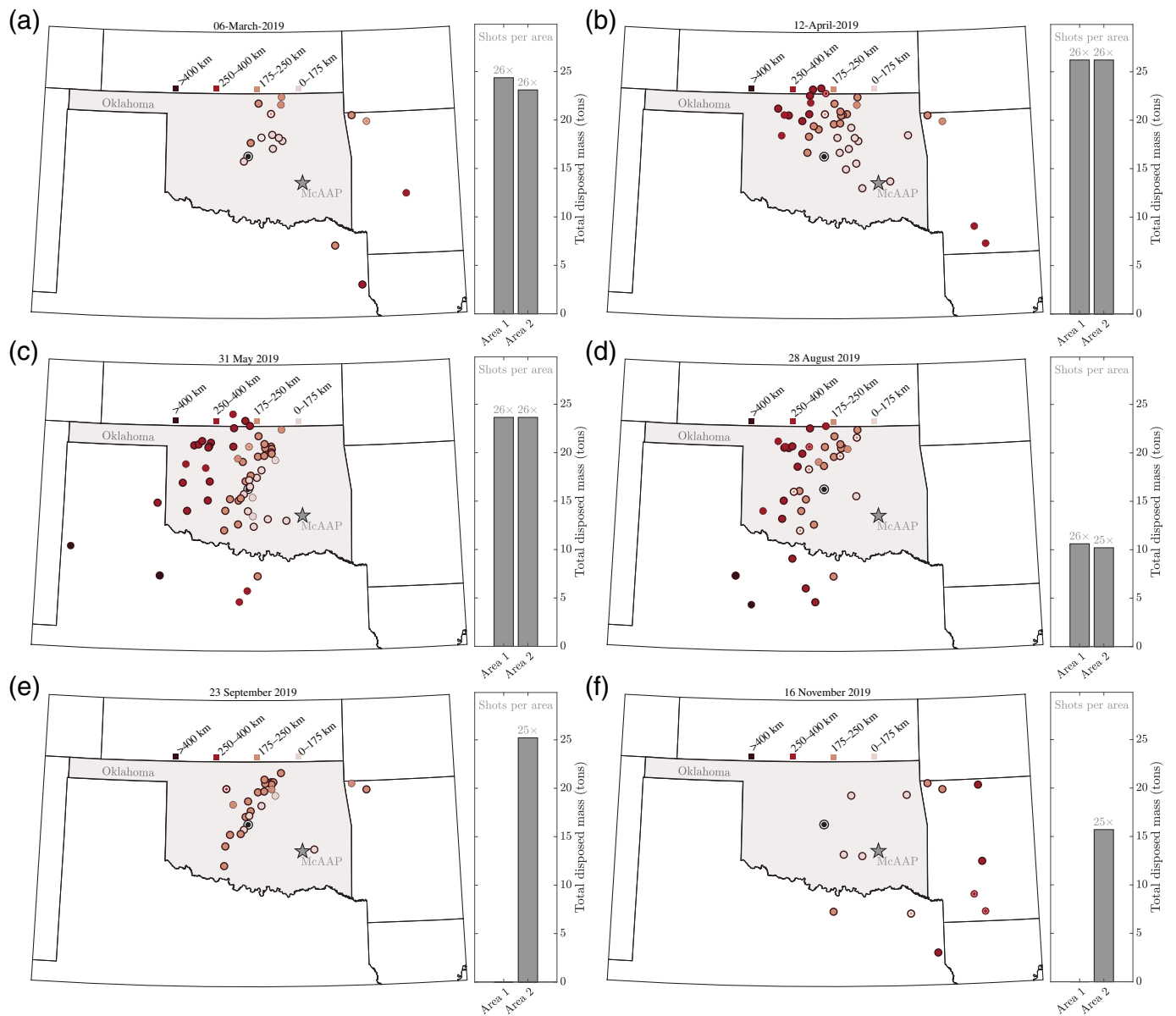
Several of these same neighbors that were unaware of the demolition activities at McAAP hypothesized the source of the signals to be construction activity, gas flares, earthquakes, hydraulic fracturing, or thunder; at least two residents emphasized that the sounds did not resemble those from fireworks. Several residents thought that the sound source was underground, which invited a response from another resident that they did not interpret the source as underground. It was unclear if the signals presented a nuisance to these residents, although observer A and a large fraction of these neighbors reported that they had witnessed similar "booms" in previous years in the neighborhood of Hidden Oaks and 4–5 yr preceding 2019.

Our own visual review counted 57 stations with visual pulse sequence observations on 18 June 2019; 45 stations on 25 June



2019; 37 stations on 21 August 2019; and 26 stations on 22 August 2019. The four stations deployed nearest the residence of observer A include OK029 (3.8 km distant), RCF53 (9.5 km distant), ARCA (17.2 km distant), and BLUF (18.0 km distant). We confidently observe pulse sequences at each of these four stations on both of days in June, although station OK029 records ambiguously overlapping pulses on 18 June 2019. Station BLUF recorded an ambiguous pulse sequence on 21 August 2019, and we confidently observe pulse sequences at the remaining three stations. On 22 August 2019, only station RCF53 (ambiguously) recorded any pulse sequence. We

Figure 7. Results from our manual, seismoacoustic waveform quality analyses. (a) The number of stations with a visible pulse sequence of any typology (vertical axis) compared against the binned fraction of the total days with any observations (horizontal axis). Station codes in each column show the set of sensors that recorded each indicated fraction of pulse sequences. In particular, we visibly identified pulse sequences of any typology on stations POCA, SC14, and MRSH during 55%–60% of days with logged blasting activity. (b) A contextual probability density function (PDF) shows the relative frequency that our visual analysis identified each indicated typology (horizontal axis). The vertical axis label N_k/N_{tot} indicates the observed frequency of a particular typology ($k =$ confident, ambiguous, overlap, or ambiguously overlapped) relative to the total number of observations N_{tot} .



conclude that residents provided more sensitive observations of pulse sequences when compared with the relative sparsity of visible seismometer records in August. This suggests that residents located near other stations that recorded pulse sequences, which we grade as “confident” to “ambiguous,” would almost certainly observe them.

Waveforms detected by noise-adaptive STA/LTA and binning algorithm

We next determined the capability of baseline, digital waveform detectors to identify pulse sequences for comparison with our manual observations and resident reports. At first, we experimented with constant-false-alarm rate (CFAR) template-matching detectors. These detectors included both network-based correlation (Carmichael and Hartse, 2016) and cone detectors (Carmichael, 2016, 2019a) that each operated with a 5 s waveform template that we extracted from a pulse sequence and

Figure 8. Maps (a)–(f) show visually graded seismoacoustic pulse sequence detections from late winter (6 March 2019), through mid-autumn (16 November 2019), paired with cumulative mass destroyed at each of the disposal areas (right bar plots, each panel). Thick circular borders indicate confident observations of the pulse sequence; light borders indicate ambiguous observations. Superimposed circles indicate overlapping observations of pulse sequences that likely indicate acoustic multipathing through the atmosphere. Light superimposed circles analogously mark pulse signals with ambiguous overlap. Labels atop each bar plot show the number of shots that McAAP conducted that day per blasting area, and the bar heights show the cumulative mass destroyed in the explosions. Each panel’s legend maps station colors to distance from McAAP. Our Supplement S2 video (2:49 in duration) animates pulse detections for each of the 169 days of documented blasting, as observable pulses track from (a) east, (b) to northwest, (c) to west, (d) to southwest, (e) subject to some variability, and (f) then back east. (a) Operations on 1 March resulted in few pulse sequence observations but destroyed over 45 t of mass, (d) whereas operations on 28 August resulted in relatively widespread observations, and destroyed only 20 t of mass, and suggest that winter versus summer meteorological conditions can exercise more control over pulse observability than yield.

scanned against data that also recorded pulse sequences. Both detectors automatically adjusted their thresholds to current noise conditions to maintain a CFAR. These algorithms gave marginal-to-fair performance, however. In particular, our detectors revealed that waveforms within individual pulse sequences showed substantial variability and low time–bandwidth product, and thereby formed poor candidates for template matching (such methods might provide superior performance against infrasound array observations). We, therefore, applied a CFAR power detector that we supplemented with a subsequent time-binning operation instead, which did not depend on any pulse-to-pulse waveform similarity. This two-stage method first selected all available vertical channel seismic data and some infrasound data within a station-specific time window. The start time of this window coincided with the earliest expected tropospheric arrival from McAAP to each station (assuming celerity $c_p < 345$ m/s), minus the expected full pulse sequence duration. The end of this time window coincided with the time duration of the expected full pulse sequence, plus the latest expected stratospheric arrival (assuming celerity $c_p > 240$ m/s), and plus the expected full pulse sequence duration. Almost all processing time windows spanned a minimum of 2400 s to a maximum of 4680 s; 11 of the 4057 Seismic Analysis Code (SAC) files available from IRIS via MATLAB function `irisFetch.m` were shorter than 2400 s. Prior to processing each seismogram with our detector, we filtered their time series with a four-pole, 5–15 Hz band-pass Butterworth filter to match the operations that preceded our visual waveform review. The first stage of our method then processed these data with an STA/LTA waveform detector that adapted its threshold in each ≤ 2400 s processing window to maintain a CFAR of $\text{Pr}_{FA} = 10^{-3}$ (Fig. 9b,e). In detail, this detector calculates the short-term average to long-term average (STA/LTA) statistic from two quasi-independent estimates of sample variance $\hat{\sigma}^2$ at each time index in a data stream, in which such ratios are well defined, and uses this statistic as a pointwise, asymmetric measure of data SNR (Fig. 9a,d). Probability theory predicts that such STA/LTA statistics have scaled F -distributions that quantify the performance of the progenitor detector (Carmichael and Nemzek, 2019). During processing, our algorithm estimates the scaled, central- F probability density function (PDF) parameters that best fit the middle 97.5% of this binned data in a least-squares sense. The algorithm then uses these parameters to specify the inverse, central- F cumulative distribution function (CDF) of the STA/LTA statistic and computes a detection threshold from the CFAR constraint (Fig. 9c,f); this detector algorithm updates thresholds every ≤ 2400 s to accommodate temporally variable noise conditions. If the STA/LTA statistic does exceed its threshold for a prescribed number of samples, our algorithm declares an event (whether on signal or noise) at the time index that marks the maximum statistic and “turns off” for a set sample duration to avoid redundantly triggering on the same waveform.

The second stage of our detection scheme bins the detection time output from the STA/LTA detector algorithm to identify sets of waveforms separated in onset by integer multiples of 20 s, up to and including 480 s (20 s/pulse \times 24 pulses). To capture variability in pulse repetition times and to reduce pulse miss rates, we accepted absolute detection times that differed from our predictions by ≤ 4.5 s, so that a time bin centered at 20 s had edges at 15.5 and 24.5 s. When this resultant binning captured four or more pulses, we identified this set of waveform detections as a pulse sequence, consistent with our visual review. This binning scheme, therefore, accepted four to n detections ($4 \leq n \leq 24$) with pick times in the set $[t_0 - n\Delta t - \varepsilon, t_0 + n\Delta t + \varepsilon]$, in which $\Delta t = 20$ s, with error $|\varepsilon| < 4.5$ s. The Appendix quantifies detection probabilities of pulse sequences and describes efficient implementation of pulse binning.

We applied our two-stage detector against each day that McAAP documented blasting and to each sensor record that we manually confirmed to contain pulse sequences. To estimate false trigger rates on pulse sequences, we also applied our detector to ~ 4800 s seismograms recorded at least 1.5 hr prior to documented blasting operations (at 14:30 or 15:30 UTC, depending on daylight savings). This scheme, thereby, produced two sets of pulse sequence detections: The first set includes detections from time intervals that we could visibly confirm contained pulse observations, and the second set includes false detections from earlier time intervals that seismic stations should have not recorded any pulse sequences sourced by explosions at McAAP.

STA/LTA detections versus ground truth

We estimate the true pulse identification rate of both full and partial sequences with our two-stage detector and three datasets: (1) our blast log data, (2) detections output during days with logged blasting, and (3) false detection rates that we estimated from time periods with no logged blasting. Symbolically, our digitized blast log data documents N_{GT} shots (GT indicates ground truth), and our two-stage detector outputs N_D detection counts per processing time T_D on a particular day. This same detector also outputs N_{FA} detection counts per processing time T_{FA} during periods with no logged blasting on the same day. We then define the number of detector counts on a candidate pulse sequence, less expected number of counts on background data as the “empirical detection probability.” An estimate of this empirical detection probability $\hat{\text{Pr}}(D)$ of our algorithm against data that records pulse sequences from a single day is then:

$$\hat{\text{Pr}}(D) = \min \left[1, \max \left[\frac{N_D - wN_{FA}}{N_{GT}}, 0 \right] \right], \quad (1)$$

in which weight $w = T_D/T_{FA}$ enables comparisons between detection rates measured from mismatched window lengths,

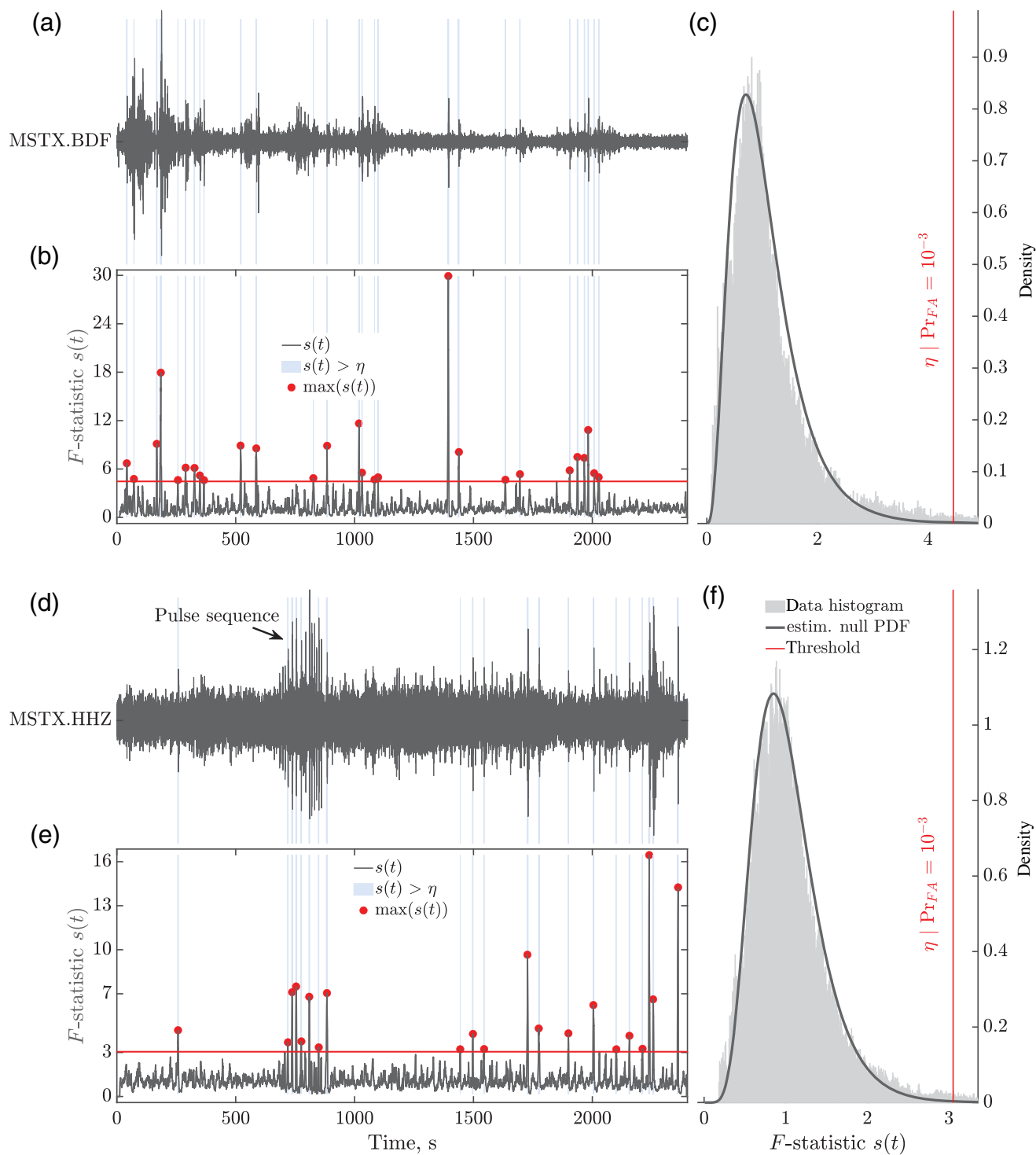
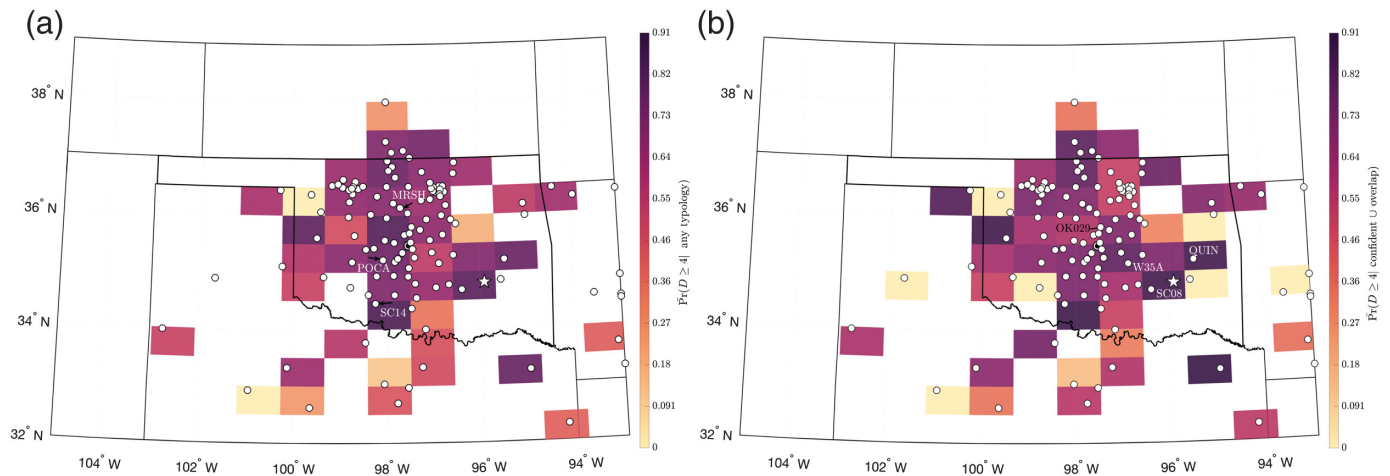


Figure 9. Summary, automatic output of a three degree of freedom short-term average to long-term average (STA/LTA) detector applied to 2400 s of data recorded after 30 April 2019 17:38:51 UTC at codeployed (a–c) infrasound and (d–f) seismic stations with code MSTX, located 640 km from McAAP. (a) Maximum-normalized infrasound records of 5–15 Hz band-pass-filtered data with channel code BDF that records a 52-pulse sequence. (b) The STA/LTA statistic $s(t)$ of the infrasound record in (a), superimposed with a threshold for event detection η that is consistent with a $\text{Pr}_{FA} = 10^{-3}$ false detection probability (notation here matches that in the Appendix). Red circles mark where this statistic exceeds η (red horizontal line). Light blue shading indicates waveforms identified by the STA/LTA

detector triggering algorithm. (c) A normalized data histogram (gray bars) of the STA/LTA statistic superimposed with the best-fit central F -PDF (black curve). The red, vertical threshold line corresponds to η in (b). The norm of the pointwise difference between the histogram and PDF curve (the bars and solid curve) defines the estimate of the F -PDF fit error. Panels (d–f) show the same features as (a–c), but for a vertical channel (HHZ) seismogram recorded at a codeployed seismic sensor. The detector captures a labeled set of pulse sequences recorded between 1800 and 2050 s. Although our analysis does not include infrasound detections, we include panels (a–c) to demonstrate that our single infrasound stations do not clearly capture the same sequences as the seismic sensor in (d,e).



hats above the probability indicate an estimate, and event D indicates that the detector identifies all pulses sourced by the N_{GT} shots. The min and max operations prevent false detection counts within a time window longer (or shorter) than the blasting window from being overcounted (or undercounted), and prevents detection rates from becoming either negative or exceeding one. We also use equation (1) to estimate empirical detection probabilities $\widehat{\Pr}(D \geq 4)$ of partial pulse sequences that include four or more consecutive pulses (event $D \geq 4$). These latter events compare with confident typologies that require four or more consecutive pulse with visible, high SNR (e.g., Figs. 6 and 7b).

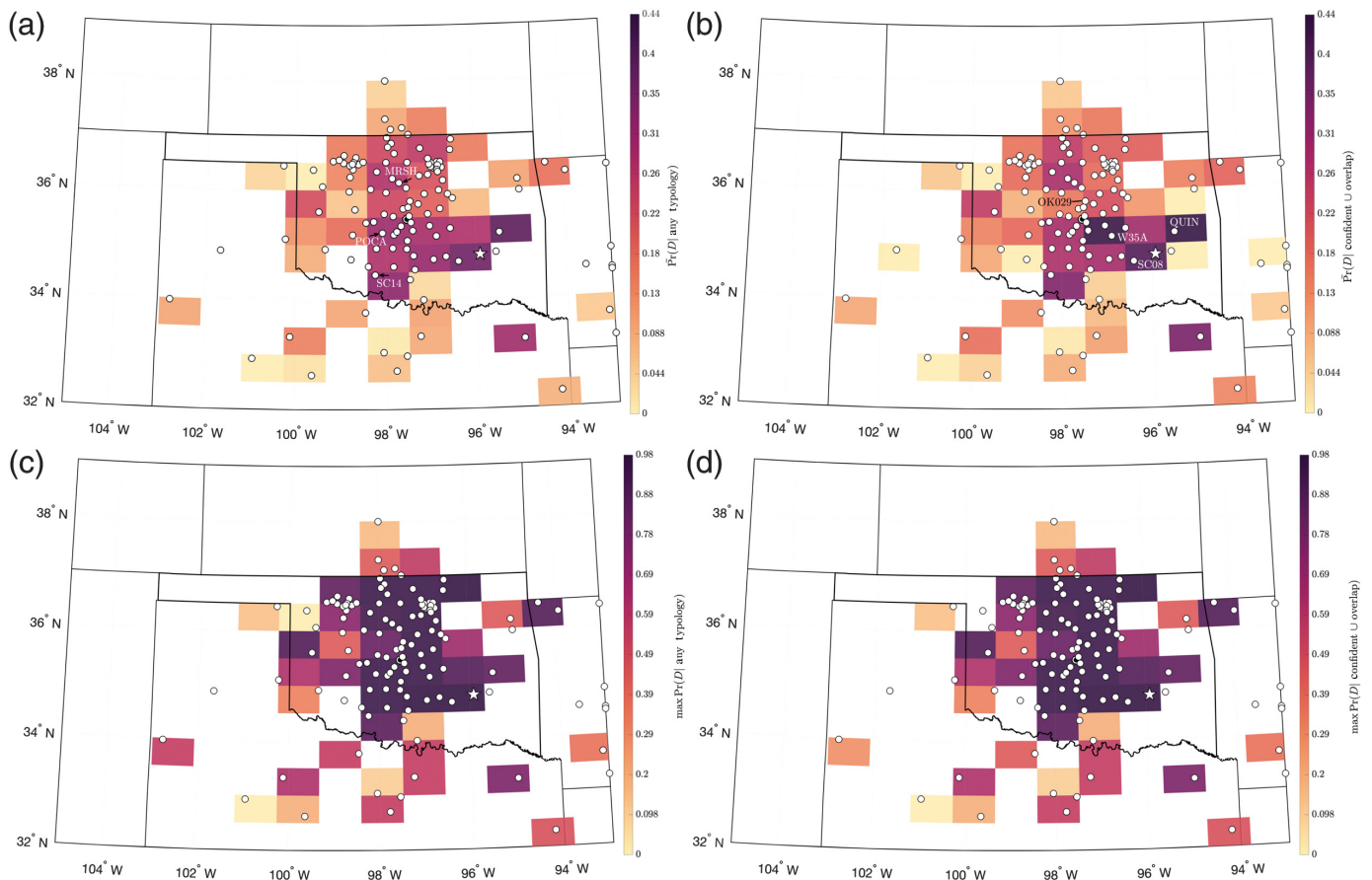
To interpret any spatial dependencies in our digital detection rates, we averaged partial pulse sequence detections over time (seasons) and within a 12×12 grid of geographical bins that covered our study region. We, thereby, averaged over pulse sequences of any visual typology grade and then over pulse sequences with either confident or overlapping typologies. These distinct averages defined unconditional detection rates (data from any typology), which we write as $\widehat{\Pr}(D|Any\ Typology)$, and conditional detection rates (data from unambiguous typologies), which we write as $\widehat{\Pr}(D|Confident \cap Overlap)$. We similarly write our estimates of unconditional detection rates on four or more pulses as $\widehat{\Pr}(D \geq 4|Any\ Typology)$, and our estimates of conditional detection rates on four or more pulses as $\widehat{\Pr}(D \geq 4|Confident \cap Overlap)$. With this notation established, our resulting, spatially binned unconditional detection rate for any pulse typology generally exceeded 0.5 ($\widehat{\Pr}(D \geq 4|Any\ Typology) > 0.5$) over a vast majority of our study region ($\leq 85\%$ of bins). In particular, our detector shows good qualitative agreement in geographical bins that host stations with relatively large fractions of visibly confirmed pulse sequences (POCA, SC14, and MRSU; Fig. 10a). Conditional detection rates $\widehat{\Pr}(D \geq 4|Confident \cap Overlap)$ that included only unambiguously graded typologies of pulse sequences showed an expected increase in observed rates. Station QUIN located southeast of McAAP shows the greatest detection rate

Figure 10. The spatially averaged, mean probability that our two-stage detection scheme identifies four or more consecutive pulses sourced by McAAP, (a) unconditional on typology, and (b) conditional on typology. Background maps use the same format as Figure 7 and include observations over the entire 18 February to 20 November 2019 observation period. These data empirically exclude false detection rate estimates (equation 1). The star marks McAAP, the capitol marker shows OKC, and the white circles show 120 seismic stations with at least one pulse sequence observation of any typology. Station code labels mark sensors mentioned in the [STALTA Detections versus Ground Truth](#) section. (a) The probability that our two-stage detector declares the presence of four or more McAAP-sourced consecutive pulses, unconditional on manual observation typology, averaged over the total observation period, and binned by geographical location. The color of each $0.5^\circ \times \sim 0.92^\circ$ latitude-by-longitude bin shows mean detection probability. (b) The same as (a) but with conditional detection probability estimates. In this case, spatial-temporal averages include only unambiguous manual pulse sequence observations.

(Fig. 10b) but was only deployed after 22 October 2019. Overall, geographical regions with dense sensor deployments located about 150–300 km west of McAAP, and some outliers (like QUIN), show detection probabilities that qualitatively reproduce our manual, confident observations.

These manual observations of partial pulse sequences poorly represent unconditional, digital detection rates of full pulse sequences ($\widehat{\Pr}(D|Any\ Typology) < 0.44$; Fig. 11a). However, sensors deployed within 100 km of McAAP (SC08, QUIN, and W35A) provide higher conditional detection rates on full pulse sequences ($\widehat{\Pr}(D|Confident \cap Overlap)$; Fig. 11b). This does not mean that the geographical bins that contain these stations provide more digital detections on either partial or full pulse sequences, when compared with other stations. Rather, this success rate indicates that if a pulse sequence was visibly observable at those particular bins within 100 km, then a detector is more likely to trigger on every pulse within that sequence.

We next found the maximum probability that any station within a geographical bin detected a full pulse sequence. This is equivalent to the expected rate that any station, at any time within each region, detected every pulse sourced at McAAP on a



given day. Our data indicate that 12 such bins that contain 63% of the 120 stations achieve at least a 0.8 maximum probability of detecting such pulses (Fig. 11c). The maximum probability of detecting every pulse amongst events with only unambiguous manual pulse observations (Confident \cap Overlap) show identical statistics, despite subtle differences in detection rates (Fig. 11d). These statistics indicate that a clear majority of the sensors within our study region will likely record a full pulse sequence sourced at McAAP at least once a year, as long as propagation conditions and operational activity during 2019 grossly represents path conditions and disposal operations at other times.

INTERPRETATIONS AND DISCUSSION

We compared the variability of seismoacoustic observations of pulse sequences sourced by McAAP against two basic source parameters: explosion size and date. Our visual observations confirm that pulse observability generally increased with net explosive yield, at least, when viewed at coarse temporal and spatial resolutions (Fig. 5b). In contrast, high temporal resolution maps show that the observability of these pulses is relatively independent of net explosive yield, especially during the late spring and summer months (Fig. 8). Relatively large disposal operations that destroyed 52 t of mass per day were, at times, invisible on all but two stations (9 April 2019, Supplement S2, time 0:28). Small disposal operations that

Figure 11. The spatially averaged, (a,b) mean and (c,d) maximum probability that our two-stage detection scheme identifies a full pulse sequence pattern that is sourced by McAAP, (a,c) unconditional on typology, and (b,d) conditional on typology. Figure format matches that of Figure 10, and station labels mark sensors discussed in the *STA/LTA Detections versus Ground Truth* section. (a) The probability that our two-stage detector declares the presence of all McAAP-sourced consecutive pulses, unconditional on manual observation typology, averaged over the total observation period, and binned by geographical location. The color of each $0.5^\circ \times \sim 0.92^\circ$ latitude-by-longitude bin shows mean detection probability. (b) The same as (a), but with conditional detection probability estimates. In this case, spatial-temporal averages include only unambiguous manual pulse sequence observations. (c) The maximum probability that our two-stage detector declares the presence of a pulse sequence that is unconditional on manual observation typology, at any sensor and time, and binned over region. (d) The same as (c) but using the conditional probabilities selected for (b). Geographical bins present in (a), (c), or (d) that are present in (b) indicate where false detections on background seismicity exceed mean (or max) pulse detection rates in (a), (c), or (d).

destroyed ≤ 5 t of mass on a given day were also, at times, visibly recorded on up to 30 stations (9 July 2019, Supplement S2, time 1:20), including one station ≤ 400 km from McAAP. Our data include other examples in which pulse sequences sourced by small yield shots were more observable than pulse sequences sourced by larger shots. We reviewed both FAA weather data (Supplement S1, Sheet A) and tornado statistics (Supplement S3) over both April and July, and found no anomalous weather

patterns that could drive broad area, elevated winds to explain the relative differences in pulse observability. Similarly, we reviewed background noise variance estimates that the first stage of our STA/LTA detector output at station PERY, for days in July and April, and found that noise energy was comparable between dates and times with dissimilar detection rates. This suggests that noise disparities at different stations could not generally explain differences in pulse observability, and that explosive size is, therefore, an unreliable predictor of the spatial extent of day-to-day pulse observability. Most such positively observed pulse sequences, in fact, provide high SNR—confident observations of waveforms that record between four and 52 consecutive shots (Fig. 5a). Unambiguously interleaved pulse arrivals (8% of observations; Fig. 5a) that indicate multipathing through the atmosphere (Fig. 6, blue marker) are entirely absent from the most seismic stations (~62%), but are substantially present on others (e.g., 31% of 98 observable days at SC14). Other stations recorded almost exclusively unambiguous pulse sequence observations (X34A), whereas others almost exclusively recorded ambiguous arrivals (DEOK) (Supplement S1, Sheet B). These data collectively indicate that low temporal and spatial resolution seismoacoustic observations of pulse sequences do not represent the higher resolution processes that individual stations or geographical regions record. That is, these average observations do not necessarily indicate observations of the average.

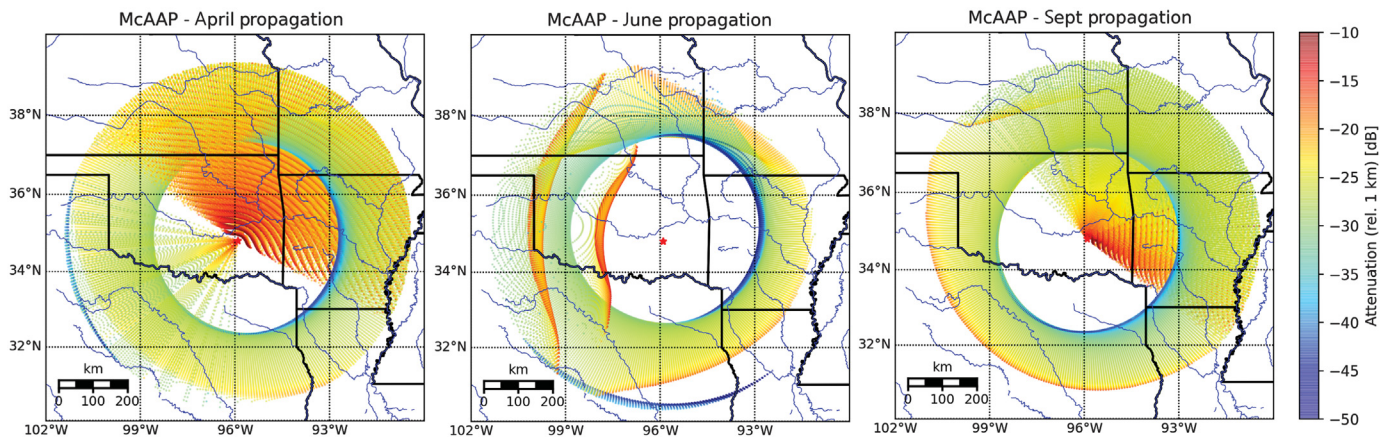
Spatial and temporal variability

A clear majority of sensors that record explosions sourced at McAAP between May and September locate to the west of McAAP (toward OKC). In contrast, sparse sensor deployments east of McAAP record their dominant fraction of pulses in late winter to early spring or in late summer to autumn. Higher fidelity animations of visible pulse sequence observations (regardless of typology) that progress from March through November show a clear spatial evolution of ostensible infrasound ground arrivals that cluster east in winter and spring, then west in spring and summer, southwest in late summer and fall, and which finally reverse direction eastward (Supplement S2). These spatial and temporal observations are consistent with those made by de Groot-Hedlin and Hedlin (2015) using triads of infrasound arrays deployed across the United States within the Transportable Array. In that work, the authors interpreted the temporal change in ground arrivals to indicate a shift in zonal stratospheric winds that enable favorable propagation of acoustic energy through a waveguide to the more westerly sensors in the direction of those winds. These winds are also seasonally stable and mostly present from mid-May through August in the contiguous United States. Lower altitude tropospheric winds (the jet stream) then enable the formation of infrasonic waveguides to the east by mid-September. In contrast to stratospheric winds, the appearance of these waveguides show seasonal variability on time scales of about a week. These waveguides can also turn

north or south earlier than seasonal averages predict, can weaken with reduced wind strength, or disappear altogether for multiple days. In particular, Blom *et al.* (2018) showed that ground sources of infrasound located near Dallas (250 km from McAAP), and excited during the spring, follow ray paths with slow celerity arrivals that transverse the thermosphere, and include some intermittent (faster) tropospheric paths. This latter analysis included 10 yr of ground-to-space (G2S) atmospheric specifications (see Schwaiger *et al.*, 2019) and raytracing analysis to also conclude that the rays from even small shots have a high probability of being refracted groundward due to the westward stratospheric waveguide that exists from May through August. More recent work by Blom and Waxler (2021) showed that only low-frequency (0.1–0.4 Hz) energy well below the passband of our digital filters (5–15 Hz) is likely to be observed from these spring time, thermospheric arrivals.

To better determine if the pattern of infrasound arrivals within our seismometer network matched the atmospheric processes outlined by de Groot-Hedlin and Hedlin (2015), Blom *et al.* (2018), and Blom and Waxler (2021), we computed a rolling, two-week weighted average of sensor azimuths that record pulse sequences of any typology (the azimuth center of mass). We computed these azimuths relative to the linear axis of area 2 to exploit a physical feature with a characteristic orientation in our analysis. The product of the fractional number of pulse sequences that we observed relative to the number of shots logged on a given day and the inverse number of stations within that same azimuthal bin formed our averaging weights. This weighting included network geometry and reduced spatial sampling bias, and we omitted data without observations (like Sundays). The resultant computation produced a time series that captured a concentration of infrasound arrivals east of McAAP in late winter and spring, followed by azimuthally stable arrivals northwest of McAAP during the spring and summer, and ending with a southwest concentration of arrivals during autumn, before trending eastward again (Fig. 12). These data are consistent with our interpretation that stable, summertime ground intercepts are largely driven by westward stratospheric winds, whereas tropospheric ducting creates waveguides that enable more variable eastern and southern ground intercepts outside of summer.

We next used the physics-based, eikonal equation solver (infraGA) to determine if the hypothesized tropospheric waveguides can qualitatively explain the infrasonic arrivals out to 500 km from McAAP, in certain cases. This numerical package solves the fluid mechanical equations that govern acoustic propagation through a spherical atmosphere in the geometric (ray-theory) limit, within a G2S-specified atmospheric model, which uses weather data and climate models to estimate atmospheric specification updates every four hours. This solver is computationally expensive on dense grids, and we, therefore, limit a full propagation analysis to only three significant days (12 April 2019, 18 June 2019, and 25 September 2019). We



selected 12 April 2019 to match spring observations in Figure 8a, 18 June 2019 to match residential observations reported over social media (Fig. 2), and 25 September 2019 to review the last day with far-west visual pulse sequence observations (including SMWD and MSTX). Results from these simulations highlight significant differences in propagation characteristics (Fig. 13). Arrivals from McAAP predicted during 12 April show a strong tropospheric waveguide to the northeast and some boundary layer ducting to the southwest. A large symmetric ring of arrivals about 300 km from McAAP shows thermospheric paths that our data were unlikely to record in our processing passband. The pattern of relatively high-energy arrivals (Fig. 13, yellow-to-red markers) match the general distribution of visible arrivals in Figure 8a. Arrivals from McAAP predicted during 18 June 2019 show a lens-shaped feature that indicates multiple arrivals from stratospheric paths that is spatially coincident with populated areas near OKC. We note that our animation (Supplement S2, time 1:05) shows several visibly overlapping arrivals that are consistent with stratospheric pairing (Waxler *et al.*, 2015; Blom, 2019) and ambiguously overlapping arrivals on 18 June 2019. The approximately circularly region with absent ground arrivals depicts the classical stratospheric shadow zone (Negaru *et al.*, 2010) and spatially coincides (roughly) with a relative absence of confident pulse sequence observations at stations ≤ 175 km from McAAP. Finally, our 25 September 2019 predictions show a tropospheric waveguide to the east and southwest that may explain sensor observations in that direction. Our confident visual observation of an overlapped pulse sequence at SMWD in north Texas, 260 km from McAAP (Supplement S2, time 2:17), is also spatially consistent with a ring of relatively high-energy arrivals (Fig. 13, yellow-to-red markers). We note that our predictions of the boundary layer duct in the north that we do not observe in our data may be overestimated due to the relatively high-frequency passband we use in our data analysis. Some pulse sequence observations also appear at stations farther west and south than we predict, and we concede that the true waveguide may have a more southward orientation than our models show.

Figure 12. Infrasound ground arrivals predicted by infraGA for a source located at McAAP (red star) on 12 April 2019 (left), 18 June 2019 (middle), and 25 September 2019 (right). In each case, the blue ring centered about McAAP shows thermospheric returns that we interpret from accompanying, turning height estimates for each ray (not shown). The *Spatial and Temporal Variability* section in the article documents our interpretation of the other various ground return features colored in each panel, which we omit here for space.

Although limited, we can conclude that the spatial patterns of our visual pulse sequence observations qualitatively agree with the physics-based propagation arrivals predicted by infraGA. We, therefore, assert that tropospheric waveguides present in the east during spring and fall, as well as stratospheric ducting of infrasound energy to the west during summer months, contribute to the temporal variability of our observations.

Residential observations

Our infraGA model predications strongly indicate that stratospherically ducted signals explain spatially dense observations of pulse sequences west of McAAP during the late spring and mid-summer. This coincidence, and our high probability, digital pulse sequence detection rates (Figs. 10 and 11), likely explain the pervasive residential reports of “banging” noises ~ 170 km westward from McAAP (Fig. 2). Although we cannot make an assessment of the pulse amplitudes or characteristics from anecdotal observations, we attempt to explain why indoor residents observed these signals over the reported sounds of their dogs, toddlers, and appliances, even when seismometers did not. In our conceptual model, a near-planar wavefront defined by a perturbation Δp in the atmospheric pressure field arrives at the exterior wall of residential house of area A and makes a shallow angle θ with the outward normal of that wall. The net force exerted on the external wall by each pulse in a sequence sourced by McAAP is then $\Delta F = \Delta p A \cos \theta$. We conservatively estimate exterior resident walls have dimensions $\sim 10 \text{ m} \times 3 \text{ m}$. Modeling work (Blixt *et al.*, 2019; Fig. 5) suggests that most of the energy within infrasonic arrivals from ground sources intercept downrange receivers 170–180 km from source at shallow angles of about 10° – 15° . This means that

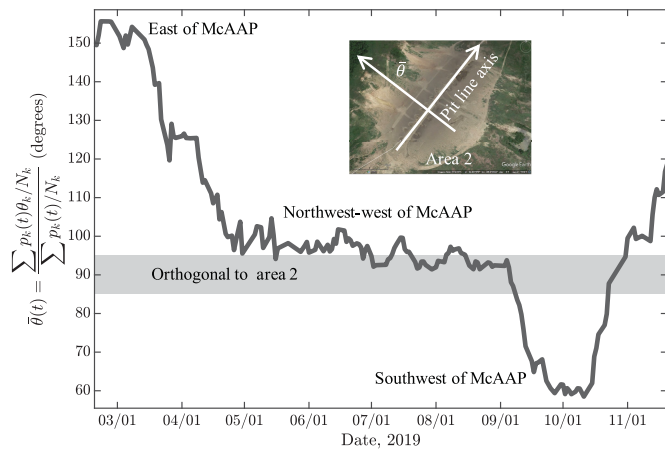


Figure 13. The “center-of-mass” azimuth of visually confirmed seismoacoustic arrivals from McAAP (vertical axis) versus blasting date (horizontal axis) over a ~10-month period. Probability $p_k(t)$ indicates the relative temporal frequency of observations of a pulse sequence observation at stations within bin k . These probabilities weight each azimuthal value θ_k in that bin, and the number of station detections N_k inversely weight the same bin (index k ranges of bin). (Inset) The definition of azimuth, relative to the linear axis of area 2, so that is orthogonal to the area 2 axis. The dark curve shows a moving, two-week moving average of θ . The peaks and troughs likely correspond to changes in the structure of tropospheric waveguides outside of summer, whereas the late spring through summer trends corresponds to stable, east-to-west stratospheric winds. The gray bar indicates a 10° bin width that is centered at 90° (orthogonal to pit axis). All angle values are phase-wrapped to positive angles ($0^\circ \leq \theta \leq 360^\circ$). Dates are labeled as month/day.

$\cos \theta > 0.96$, and that we can assume that $\cos \theta$ is effectively one. Collectively, we estimate that $\Delta F \sim 30 \text{ m}^2 \Delta p$. Residential homes, therefore, act like transfer functions between pressure pulses of the shallowly arriving acoustic wavefronts sourced at McAAP and directed forces against their exterior walls, which amplify signals by $\sim 30\times$. Grazing-angle infrasound returns at seismometer locations on flat ground do not record such amplification. We, therefore, suggest that stations installed may provide more sensitive records of seismoacoustic signals when infrasound ground intercepts are shallow.

Spatially and temporally averaged empirical detection probabilities

Operators of disposal sites such as McAAP remain concerned with noise abatement strategies, and actively seek automated and predictive methods to quantify the probability that residents (such as those in Edmond, OK) will witness pulses sourced by their operations (Calderone and Garbin, 2001). We assert that seismic network data that are automatically processed with augmented, noise-adaptive STA/LTA algorithms provide average pulse sequence detection probabilities that reasonably represent visual observation rates, which can serve as a proxy for residential observation rates. Although our results show that such averages appear more useful for predicting partial pulse sequences

(Fig. 10) rather than full pulse sequences (Fig. 11a,b), operator discretion determines what value of mean or maximum detection probabilities require extra abatement efforts. We, therefore, consider each case here.

Our two-stage detector first identified partial sequences composed of four or more visually identifiable pulses at > 0.5 probability, over $> 63\%$ of our 144 geographical bins (Fig. 10a). If we restrict our estimates to pulse sequences with confident visual observations (which includes overlapping sequences), we achieve the same detection rate on $> 68\%$ of geographical bins (Fig. 10b). Regions 170–220 km that often include dense sensor deployments and residential populations (e.g., OKC) often show bin-specific, time-averaged detection probabilities as high as > 0.85 (any typology) and > 0.88 (confident typologies). Some isolated regions with single stations showed even higher detection values (e.g., SC08 and QUIN). Detection rates averages that include data from station OK029 near observer A, in particular, record values of about 0.65, suggesting that observers near sensors such as SC08 and QUIN are even more likely to witness blasting activity than those in Edmond, OK.

The detector identified full pulse sequences sourced at McAAP with a much lower mean probability. Detection rates of full pulse sequences of any typology at latitudes directly south of OKC showed an average of about 0.25 (Fig. 12a), and peaked at about 0.4 at stations closer to McAAP such as QUIN, W35A, and SC08. These values are slightly higher for pulse typologies with confident visual observations (Fig. 12b). We emphasize that our ground-truth dataset does not screen partial sequences of four or more pulses from full pulse sequences. Therefore, our detection results here may simply reflect that some pulses sourced by McAAP shots were not observable above noise, visually or digitally.

Maximum detection probabilities of full pulse sequences appear to provide particularly good agreement with our visual observations of partial pulse sequences, in a majority of geographical bins (Fig. 12c,d). That is, our detector shows a very high probability ($0.8 < \max\{\widehat{\Pr}(D|\text{Any Typology})\} < 0.98$) of identifying a full pulse sequence within most geographical bins at least once during our nine-month study period, given that we visually confirmed that a seismometer recorded a pulse sequence within that same bin. These rates are higher for sequences with confident visual observations. These maximum probabilities peak over a bulk $2.5^\circ \times 1.8^\circ$ latitude-by-longitude region of 10 adjacent geographical bins that cover OKC and show that sensors in this (relatively) population dense region will almost certainly record a full sequence of pulses sourced at McAAP.

We conclude that automated processing of seismic data with noise adaptive detection and binning schemes provide probabilities that underestimate the seismoacoustic observability of McAAP blasting activity. Anecdotal (but voluminous) first- and third-party witness reports delivered by observer A, coupled with the absent-to-confident visual typologies that we graded from nearby seismometers, further suggest that indoor residents

can observe pulse sequences that some seismometers do not record above noise. On average, we expect our digital detector to identify about 65% of these sequences. In words, we suggest that human observers, under some conditions, are more sensitive to seismoacoustic signatures of blasting activity than seismic analysts, which are more sensitive than partially automated digital waveform detectors. We emphasize that this inequality assumes that observer A and their neighbors represent typical witnesses, and is therefore subject to poorly known caveats.

The observability of single pulses sourced at McAAP

Our two-stage pulse sequence detection algorithm requires that an STA/LTA detector trigger on at least four consecutive pulses separated by approximately 20 s and, therefore, cannot directly quantify the expected rate that an observer records a signal pulse. We can use our data, however, to invert for the average probability that our detection system will identify a single waveform within a given pulse sequence. To compute this inversion, we use the CDF that quantifies the probability $\Pr(D \geq d | \text{Consec})$ that an observer records at least D consecutive pulses from $4 \leq N \leq 47$ possible shots, if the probability p of a single-pulse detection is known:

$$\Pr(D \geq d | \text{Consec}) = 1 - \frac{(1 - px)/(1 - p)}{(d + 1 - dx)} x^{-(n+1)}. \quad (2)$$

The notation of equation (2) indicates that D is the random variable describing consecutive STA/LTA pulse detections, and x is the real-valued root of $V(x) = 1 - x + (1 - p)p^d x^{d+1}$ that is not $1/p$ (Feller, 1957, p. 325). To invert for p , we set equations (1) and (2) ($\hat{\Pr}(D > d) = \Pr(D > d | \text{Consec})$), $N = N_{\text{GT}}$, and use the value of $d \geq 4$ output from the second stage of our detector at each sensor, for each day. We then averaged these pulse detection probability estimates that we write as \hat{p} over time, and binned them into the same geographical regions that we used to estimate partial and full pulse sequence detection rates. We emphasize that our binned estimates are conditioned on the event that our two-stage detector first identifies a pulse sequence and accounts for false detections. This average over time, space, and over four-to-47 pulses, therefore, provides a low-resolution, robust estimate of the mean pulse detection probability.

Figure 14 indicates that nine geographical regions that include seismometers show a fair-to-good probability ($\hat{p} \geq 0.5$) of recording a McAAP-sourced waveform within a pulse sequence on any given day. Stations SC14, SC08, QUIN, and Z38B provide the highest chance of observing such waveforms ($0.55 \leq \hat{p} \leq 0.65$). This further suggests that blasting operations at McAAP will produce observable signals at sensors in those regions most days that such blasting occurs. We, therefore, conclude that indoor residents in those regions have a greater than 50–50 chance of observing at least one pulse from McAAP blasting activity, each day that blasting occurs, after accounting for possible false alarms sourced by noise or background seismicity.

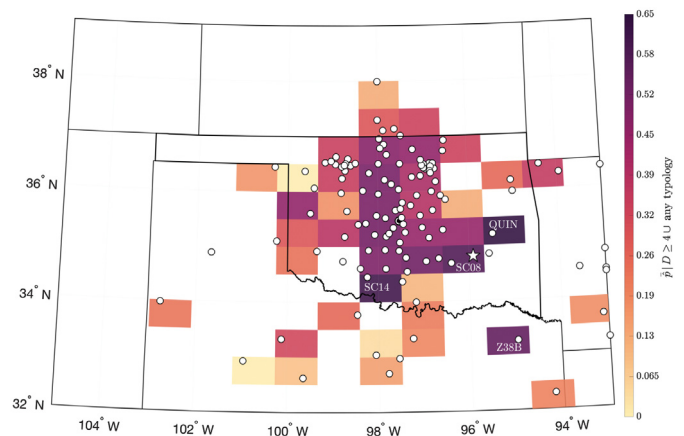


Figure 14. The spatially and temporally averaged probability that our two-stage detector triggers on a single waveform within a sequence of four to 47 pulses, which is detected by our two-stage detection system. Limited residential reports suggest that these single-pulse detection probabilities form lower bounds on the expected detection rate of a human observer.

Data retrieval issues

We often retrieved inconsistent volume of SAC files that we requested from IRIS. This means that our manual (visual) observations of seismograms occasionally included data that our batch processing could not include. In particular, the Python toolbox ObsPy retrieved an inconsistent number of files when we applied Federation of Digital Seismograph Network tools, and file retrieval rates seemed to depend on the time of day that we requested these files. We observed similar behavior from the MATLAB function `irisFetch.m`, but it seemed to provide slightly more stable behavior. We, therefore, made multiple batch data requests with `irisFetch.m` in an attempt to accumulate a higher return volume of SAC files. Our Supplement S1 illustrates a times series of such return volumes (Sheet B, Fig. S1-2). We additionally found, if we requested data with a fixed temporal width from a given day, that we sometimes obtained output with some temporal nonuniformity. We, therefore, modified our detection rate calculation to accommodate nonuniform preblasting seismicity versus postblasting seismicity (see weight function w in equation 1). Our analyses did not otherwise quantify mismatches in file volume when we computed unconditional or conditional detection rates. However, the comparison between preshot versus postshot time file retrieval indicates that some days showed a discrepancy of four stations. This preshot versus postshot difference averaged to zero over the total time period, and we, therefore, suggest that this error does not substantively affect our conclusions.

CONCLUSIONS

We provide three major contributions from a seismoacoustic study of munition disposal activity at the McAAP that had previously been incompletely explained.

Our first major contribution includes a ground-truth dataset documenting blast-log information, concurrent weather conditions, visual pulse observations, and a variety of visually graded data that two teams of analysts collected against thousands of vertical channel seismograms. The dataset format is easily accessible for subsequent atmospheric studies of propagation variability over the Great Plains, which was far outside the scope of this study.

Our second major contribution demonstrates that a composite seismometer network can record changes in spatial-temporal patterns in stratospheric and tropospheric winds, and without the inclusion of infrasound arrays. Although explosion size did control the low-resolution observability of pulse sequences over the entire nine-month observation period, high-resolution manual observations revealed that variability was largely independent of explosion size or noise variance. Spatial patterns of these ground arrivals further agree with those that we predict from the physics-based numerical modeling and suggest that stratospheric ducting of infrasound energy to the west during summer months likely contributes to the relative independence of pulse observability from shot mass.

Our third major contribution asserts that partially automated and augmented STA/LTA detectors that process vertical channel seismic network data roughly predict pulse sequence observability. These data can, therefore, show blasting operators when and where blasting activity is more likely to produce seismoacoustic signatures observable to residents. Our limited witness reports further suggest that our detection statistics underestimate observer detection rates, and that above-average digital detection rates over populated areas should indicate even higher residential observation rates.

Finally, we recommend that the seismoacoustic community exploit these disposal operations. Shots sourced at McAAP produce infrasound signals that sample the stochastic atmosphere over time scales that span 20–1200 s per day and over spatial scales that sample 30 m–2 km intershot separation distances. These data, thereby, provide a rare opportunity to use repeating infrasound waveforms as multibit signals to cheaply study multiscale physical processes over tropospheric to stratospheric altitudes, and out to regional distances (640 km) from their sources. The four-bit typology grades and digitally accessible blast records in our supplemental materials provide a ready-to-use training dataset for machine-learning algorithms that could enable such multiscale studies. Such work would support a variety of fields that include nuclear explosion monitoring, atmospheric science, and statistical physics.

DATA AND RESOURCES

Relevant metadata has been collected from Incorporated Research Institutions for Seismology (IRIS) website (<http://ds.iris.edu/gmap/>, last accessed September 2021). Supplement S1 documents a comprehensive, nine-month record of seismoacoustic observations sourced by munition disposal activity in two blasting areas (Fig. 2) that

comprise 52 distinct shot pits at McAlester Army Ammunition Plant (McAAP). The processed data resources available to the geophysical community include: digitized blast logs that contain shot time, blast number, location, and Federal Aviation Administration (FAA) weather conditions as ground truth (Supplement S1, Sheet A); manual pulse observations and typology grades for all available stations (Supplement S1, Sheet B); moveout estimates (Supplement S1, several date-tagged sheets); complete network metadata (Supplement S1, Sheet C); and an animated summary of graded pulse observations across four U.S. states, compared against shot number and mass (Supplement S2). These data provide empirical densities of source parameters (Fig. 5) and statistics for the most persistent pulse observations (Figs. 6 and 7). The Supplement S1 (Sheet B, Fig. S1-2) and Section Errors and Uncertainties document issues with accessing seismogram data that associates with our blast logs.

DECLARATION OF COMPETING INTERESTS

The authors acknowledge that there are no conflicts of interest recorded.

ACKNOWLEDGMENTS

The authors thank Steven Gibbons for alerting Joshua D. Carmichael to the acoustic anomaly; Laura Anne Mullane and Joey Montoya of Los Alamos National Laboratory (LANL) Media Relations for publicity; Maya Wei-Hass of National Geographic for national media exposure; Gideon Rogers of McAlester Ammunition Plant for facilitating access to blast log data; Sarah Terry-Cobo of the Oklahoma Corporation Commission; Omar Marcillo of Oak Ridge National Laboratory for input on infrasound propagation and technical discussions; Scott Wimer of LANL for input interpreting blast log data. Paul Smith (Observer A), a resident of Edmond, OK, provided the residential observation data that we include in our results. We generated all figures with MATLAB, v.2019a. This article has been authored with number LA-UR-21-24990 by Triad National Security under Contract with the U.S. Department of Energy, Office of Defense Nuclear Nonproliferation Research and Development. This research was funded by the National Nuclear Security Administration, Defense Nuclear Nonproliferation Research and Development (NNSA DNN R&D). The authors acknowledge important interdisciplinary collaboration with scientists and engineers from all four Department of Energy National Laboratories and their contractor partners. The U.S. Government retains and the publisher, by accepting the article for publication, acknowledges that the U.S. Government retains a nonexclusive, paid-up, irrevocable, worldwide license to publish or reproduce the published form of this article, or allow others to do so, for the U.S. Government purposes.

REFERENCES

- Albert, S., and S. J. Arrowsmith (2017). Combining seismic and acoustic event catalogs to better understand the nature of individual events, Number SAND2017-3692C, Sandia National Lab (SNL-NM), Albuquerque, New Mexico.
- Aleqabi, G. I., M. E. Wyssession, and H. A. Ghalib (2016). Characterization of seismic sources from military operations in urban terrain (MOUT): Examples from Baghdad, *Bull. Seismol. Soc. Am.* **106**, no. 1, 23–41.

- Blixt, E. M., S. P. Näsholm, S. J. Gibbons, L. G. Evers, A. J. Charlton-Perez, Y. J. Orsolini, and T. Kväerna (2019). Estimating tropospheric and stratospheric winds using infrasound from explosions, *J. Acoust. Soc. Am.* **146**, no. 2, 973–982.
- Blom, P. (2019). Modeling infrasonic propagation through a spherical atmospheric layer—Analysis of the stratospheric pair, *J. Acoust. Soc. Am.* **145**, no. 4, 2198–2208.
- Blom, P., and R. Waxler (2021). Characteristics of thermospheric infrasound predicted using ray tracing and weakly non-linear waveform analyses, *J. Acoust. Soc. Am.* **149**, no. 5, 3174–3188.
- Blom, P. S., F. K. Dannemann, and O. E. Marcillo (2018). Bayesian characterization of explosive sources using infrasonic signals, *Geophys. J. Int.* **215**, no. 1, 240–251.
- Calderone, J. J., and H. D. Garbin (2001). Demolition range noise abatement technique demonstration and evaluation for the McAlester army ammunition plant, *Sandia Report SAND2001-2267*.
- Carmichael, J., R. J. Nemzek, N. Symons, and M. Begnaud (2020). A method to fuse multiphysics waveforms and improve predictive explosion detection: Theory, experiment and performance, *Geophys. J. Int.* **222**, no. 2, 1195–1212.
- Carmichael, J. D. (2016). A waveform detector that targets template-decorrelated signals and achieves its predicted performance, part I: Demonstration with IMS data, *Bull. Seismol. Soc. Am.* **106**, no. 5, 1998–2012.
- Carmichael, J. D. (2019a). Erratum to a waveform detector that targets template-decorrelated signals and achieves its predicted performance, part I: Demonstration with IMS data, *Bull. Seismol. Soc. Am.* **109**, no. 5, 2142–2144.
- Carmichael, J. D. (2019b). What’s shaking Oklahoma? Mysterious seismic signals lead to some scientific detective work, *Scientific American*, 6 September, available at <https://blogs.scientificamerican.com/observations/whats-shaking-in-oklahoma/> (last accessed September 2021).
- Carmichael, J. D., and H. Hartse (2016). Threshold magnitudes for a multichannel correlation detector in background seismicity, *Bull. Seismol. Soc. Am.* **106**, no. 2, 478–498.
- Carmichael, J. D., and R. J. Nemzek (2019). Uncertainty in the predictive capability of detectors that process waveforms from explosions, available at <https://arxiv.org/abs/1906.09350> (last accessed September 2021).
- Carr, C. G., J. D. Carmichael, E. C. Pettit, and M. Truffer (2020). The influence of environmental microseismicity on detection and interpretation of small-magnitude events in a polar glacier setting, *J. Glaciol.* **66**, no. 259, 790–806.
- Dannemann-Dugick, F. K., B. W. Stump, P. S. Blom, O. E. Marcillo, C. T. Hayward, J. D. Carmichael, and S. Arrowsmith (2020). Evaluating factors influencing infrasonic signal detection and automatic processing performance utilizing a regional network, *J. Acoust. Soc. Am.* **148**, no. 6, 3509–3526.
- de Groot-Hedlin, C. D., and M. A. Hedlin (2015). A method for detecting and locating geophysical events using groups of arrays, *Geophys. J. Int.* **203**, no. 2, 960–971.
- Delbridge, B. G., J. D. Carmichael, R. M. Nadeau, D. R. Shelly, and R. Bürgmann (2020). Geodetic measurements of slow-slip events Southeast of Parkfield, CA, *J. Geophys. Res.* **125**, no. 5, e2019JB019059, doi: [10.1029/2019JB019059](https://doi.org/10.1029/2019JB019059).
- Edwards, W. N., D. W. Eaton, and P. G. Brown (2008). Seismic observations of meteors: Coupling theory and observations, *Rev. Geophys.* **46**, no. 4, doi: [10.1029/2007RG000253](https://doi.org/10.1029/2007RG000253).
- Feller, W. (1957). *An Introduction to Probability Theory and Its Applications*, Vol. 1, Wiley and Sons, New York, New York.
- Garcés, M. A., R. A. Hansen, and K. G. Lindquist (1998). Traveltimes for infrasonic waves propagating in a stratified atmosphere, *Geophys. J. Int.* **135**, no. 1, 255–263.
- Kitov, I. O., J. R. Murphy, O. P. Kusnetsov, B. W. Barker, and N. I. Nedoshivin (1997). An analysis of seismic and acoustic signals measured from a series of atmospheric and near-surface explosions, *Bull. Seismol. Soc. Am.* **87**, no. 6, 1553–1562.
- Koch, C. D., and S. Arrowsmith (2019). Locating surface explosions by combining seismic and infrasound data, *Seismol. Res. Lett.* **90**, no. 4, 1619–1626.
- McKee, K., D. Fee, M. Haney, R. S. Matoza, and J. Lyons (2018). Infrasound signal detection and back azimuth estimation using ground-coupled airwaves on a seismo-acoustic sensor pair, *J. Geophys. Res.* **123**, no. 8, 6826–6844.
- Negraru, P. T., P. Golden, and E. T. Herrin (2010). Infrasound propagation in the “zone of silence”, *Seismol. Res. Lett.* **81**, no. 4, 614–624.
- Nickel, G. H., and W. A. Whitaker (1971). Distant seismic waves from a high-altitude source, *Geophys. J. Int.* **26**, nos. 1/4, 369–378.
- Schwaiger, H. F., A. M. Iezzi, and D. Fee (2019). AVO-G2S: A modified, open-source ground-to-space atmospheric specification for infrasound modeling, *Comput. Geosci.* **125**, 90–97.
- Thiel, A. D. (2019). An acoustic anomaly, *OK Geological Survey Field Blog*, available at <https://okgeosurvey.wordpress.com/2019/07/25/an-acoustic-anomaly/> (last accessed September 2021).
- Waxler, R., L. G. Evers, J. Assink, and P. Blom (2015). The stratospheric arrival pair in infrasound propagation, *J. Acoust. Soc. Am.* **137**, no. 4, 1846–1856.
- Wei-Haas, M. (2019). Mysterious waves have been pulsing across Oklahoma, *National Geographic*, 13 September, retrieved from <https://www.nationalgeographic.com/science/article/strange-waves-rattled-entire-state-scientists-know-why?no-cache> (last accessed February 2021).
- Williams, B. J., W. P. Brug, E. M. Casleton, E. M. Syracuse, P. S. Blom, C. S. Meierbachtol, R. J. Stead, G. A. MacLeod, A. L. Bauer, X. M. Shao, *et al.* (2021). Multiphenomenology explosion monitoring (MultiPEM): A general framework for data interpretation and yield estimation, *Geophys. J. Int.* **226**, no. 1, 14–32.
- Wirth, M. H., R. R. Blandford, and R. H. Shumway (1976). Automatic seismic array and network detection, *Bull. Seismol. Soc. Am.* **66**, no. 4, 1375–1380.

APPENDIX

The two-stage noise-adaptive, three-parameter pulse detector

Stage 1: The CFAR STA/LTA detector. We write N samples of a detrended, 5–15 Hz band-pass filtered seismic or infrasound data stream as $\mathbf{x} = [x_1, x_2, \dots, x_k, \dots, x_N]$. The first stage of our short-term average to long-term average (STA/LTA) detector estimates the variance of such preprocessed data x in two (nearly) statistically independent, nonoverlapping windows. The

first, longer time-window estimates noise variance $\hat{\sigma}_l^2(t < t_s)$ at sample l , over L consecutive samples that precede sample l :

$$\hat{\sigma}_l^2(t < t_s) = \frac{1}{L} \sum_{k=l-L}^l x^2(k\Delta t) \text{(LTA)}, \quad (\text{A1})$$

in which time $t = t_s$ is a symbolic index that separates the last short-time-window sample from the first long-time-window sample. A leading, shorter time-window estimates $\hat{\sigma}_l^2(t > t_s)$ at sample l , over S consecutive samples that proceed sample l :

$$\hat{\sigma}_l^2(t > t_s) = \frac{1}{S} \sum_{k=l}^{l+S} x^2(k\Delta t) \text{(STA)}. \quad (\text{A2})$$

Data that record a S sample length signal preceded by L samples of noise, therefore, generate a larger STA/LTA statistic than any commensurate record containing only noise of the same variance. The detector outputs a time series with a central F -distribution at each sample when Gaussian noise contaminate the data. To test the distributional form of these data and thereby assess the predictive capability of our detector, we performed binning experiments. These experiments computed normalized histograms of the postprocessed data over multiple duration time windows and days. Our experiments demonstrated that seismic noise data were characterized by stationary Gaussian statistics over temporal durations that met or exceeded 2400 s. To continually assess these statistics, we included a distributional-fit error estimation scheme within our detector. This scheme computed root mean square (rms) misfits between the STA/LTA statistic's normalized histogram and the best-fit central- F probability density function (PDF) to provide a consistent quality check between data and our signal models. We emphasize that our detector performed this assessment automatically (unsupervised). If our data were sufficiently Gaussian, we formed a binary hypothesis test that compares two distinct signal models and related distribution functions for the STA/LTA statistic. The first (null) hypothesis \mathcal{H}_0 presumes that data \mathbf{x} include only noise. The second (alternative) hypothesis \mathcal{H}_1 presumes the data \mathbf{x} include an unknown signal superimposed with noise. This test at sample l thereby takes the form (Wirth *et al.*, 1976):

$$\begin{aligned} \mathcal{H}_0 : \quad & \frac{\hat{\sigma}_l^2(t > t_s)}{\hat{\sigma}_l^2(t < t_s)} \sim c\mathcal{F}_{S,L}(0) : c, S, L \quad \text{unknown} \\ \mathcal{H}_1 : \quad & \frac{\hat{\sigma}_l^2(t > t_s)}{\hat{\sigma}_l^2(t < t_s)} \sim c\mathcal{F}_{S,L}(\lambda_l) : c, S, L, \lambda_l \quad \text{unknown} \end{aligned}, \quad (\text{A3})$$

in which $c\mathcal{F}_{S,L}(\lambda_l)$ describes a scaled, noncentral F -distribution with S and L degrees of freedom, noncentrality parameter λ_l , and scaling parameter c . Our STA/LTA detector compares these variance ratios under each hypothesis and forms a test statistic $z_l(\mathbf{x})$ at time sample index l :

$$z_l(\mathbf{x}) \triangleq \frac{\hat{\sigma}_l^2(t > t_s)}{\hat{\sigma}_l^2(t < t_s)}. \quad (\text{A4})$$

We compare $z_l(\mathbf{x})$ against a threshold to detect waveforms in noise such that we achieve a constant-false-alarm rate (CFAR) on noise. Such a threshold requires that we first correctly quantify the distributional parameters (c , S , and L) from the noise. We, thereby, write the (unscaled) PDF for z under hypothesis \mathcal{H}_j as $f_Z(z; \mathcal{H}_j)$, in which $\lambda = 0$ under \mathcal{H}_0 ($j = 0$) and $\lambda > 0$ under \mathcal{H}_1 ($j = 1$), and omit index l here on, unless it disambiguates terms. The PDF for the STA/LTA statistic z that has a scaling parameter c is then $c^{-1}f_Z(c^{-1}z; \mathcal{H}_j)$. We estimate the parameters S , L , and c that shape the curves of $c^{-1}f_Z(c^{-1}z; \mathcal{H}_j)$ in each time window from normalized histograms of our data. Specifically, our algorithm computes parameterized misfits between theoretical curves $c^{-1}f_Z(c^{-1}z; \mathcal{H}_j)$ and normalized histograms of z , and then selects the parameter triplet that minimizes this misfit. Two such parametric estimates are

$$\begin{aligned} \hat{c}, \hat{S}, \hat{L} &= \operatorname{argmax}_{c,S,L} \|\text{Hist}|_{2,5}^{95}(z) - cf_Z(z; \mathcal{H}_0)\| \\ \hat{c}, \hat{S}, \hat{L} &= \operatorname{argmax}_{c,S,L} \|\text{Hist}|_{2,5}^{95}(z) - cf_Z\left(\frac{S}{L}z; \mathcal{H}_0\right)\|. \end{aligned} \quad (\text{A5})$$

The latter computation scales z to accommodate unmodeled correlation between the short-term and long-term windows. Our detector algorithm then selects the parameter triplet $(\hat{c}, \hat{S}, \hat{L})$ that minimizes the histogram fit error $\epsilon = \min[\epsilon_1, \epsilon_2]$ to shape the null hypothesis data PDF, in which:

$$\begin{aligned} \epsilon_1 &= \|\text{Hist}|_{2,5}^{95}(z) - cf_Z(z; \mathcal{H}_0)\| \\ \epsilon_2 &= \|\text{Hist}|_{2,5}^{95}(z) - cf_Z\left(\frac{S}{L}z; \mathcal{H}_0\right)\|. \end{aligned} \quad (\text{A6})$$

This error quantifies our uncertainty in the data model in equation (A3) for our detector; if $\epsilon = \epsilon_2$, we replace the detection statistic via the rule $L^{-1}Sz \rightarrow z$ prior to subsequent processing. To then compute thresholds for detection, we parameterize the null (central- F) PDF in each processing window with the scalar triplet that fits our data (equation A6) with error ϵ and invert for value that maintains a CFAR that we write as $\text{Pr}_{FA}^{\text{Pre}}$:

$$\begin{aligned} \text{Pr}_{FA}^{\text{Pre}} &= \int_{\hat{\eta}}^{\infty} f_Z(z; \mathcal{H}_0) dz = 1 - F_Z(\hat{\eta}; \mathcal{H}_0) \quad (\text{or}) \\ \hat{\eta} &= F_Z^{-1}(1 - \text{Pr}_{FA}^{\text{Pre}}; \mathcal{H}_0). \end{aligned} \quad (\text{A7})$$

In equation (A7), $F_Z(z; \mathcal{H}_0)$ is the cumulative distribution function of z with \hat{S} and \hat{L} degrees of freedom, and $F_Z^{-1}(p; \mathcal{H}_0)$ is its inverse, evaluated at probability p . The noise-adaptive STA/LTA detector then declares that data \mathbf{x} contain a signal at time sample t_s when the statistic $z(\mathbf{x})$ exceeds its threshold estimate $\hat{\eta}$:

$$z(\mathbf{x}) \triangleq \frac{\hat{\sigma}^2(t > t_s)}{\hat{\sigma}^2(t < t_s)} \Delta_{\mathcal{H}_0}^{\mathcal{H}_1} \hat{\eta}. \quad (\text{A8})$$

Figure 9d provides several examples of waveform detections ($z(\mathbf{x}) > \hat{\eta}$) when \mathcal{H}_1 is true against vertical channel seismic data that include a labeled pulse sequence, at station MSTX.

In this example, our detector outputs degree of freedom parameter estimates $\hat{c}, \hat{S}, \hat{L} = 4.25, 23.6, 30.46$, the red line at $\hat{\eta} = 3.0$ is consistent with false alarm rate $\Pr_{FA}^{\text{Pre}} = 10^{-3}$, and the percent fit error is $100\% \epsilon = 9.0\%$. We do not use estimates of the predictive detection probability \Pr_D^{Pre} of our detector here, and refer to Carmichael and Nemzek (2019), Carr *et al.* (2020), and Delbridge *et al.* (2020) for further theory and examples.

Stage 2: Binning pulse detections. After our STA/LTA detector output, a set of consecutive waveform detections (pulse and possibly nonpulse), we performed a rapid binning operation on waveform detection times for each station and for each day. We first construct a grid of time bins that center at integer multiples of 20 s, and up to 480 s after each signal detection, where each bin has a 4.5 s half-width. We then compute the difference in time between this particular detection and all subsequent signal detections within 489 s of that detection time. Any detection-time differences that then fell into these bins separated by 20 s were candidate pulse sequences and defined a Boolean sequence $\mathbf{u} = [u_1, u_2, \dots, u_k, \dots, u_D]$ in which $u_k = 0$ or 1 and $k \leq D = 24$.

To count partial sequences of D or more consecutive pulses that meet our visual definition of a confident observation (see the [Manual Waveform Observations](#) section), we applied a D -point sliding-window at point k to sum D elements to the left of k , for each sequence \mathbf{u} . This sum thereby outputs a value of D if our detection time differences fell into D consecutive bins backward in time from point k . To account for left end points of \mathbf{u} in which our sum was not defined, we replaced the first $D - 1$ points with a sum from an D -point sliding window that summed values to the right of point k . This collective summing process defined a new sequence $\Sigma(\mathbf{u})$. We then declared the presence of a sequence of D or more pulses in our detection data wherever $\Sigma(\mathbf{u}) = D$. To compute the maximum number of consecutive pulses within such a declared sequence, we then counted the number of “successes,” $\Sigma(\mathbf{u}) = D$, within $\Sigma(\mathbf{u})$. We label these counts as N_D when our data record visually confirmed seismoacoustic blasting signatures and N_{FA} when our data records preceded the same blasting schedule, as written in equation (1).

Manuscript received 26 May 2021
Published online 5 October 2021